Supersymmetric chameleons and ultra-local models

Philippe Brax, Luca Alberto Rizzo, Patrick Valageas

Supersymmetric chameleons and ultra-local models

Philippe Brax, Luca Alberto Rizzo, and Patrick Valageas
Institut de Physique Théorique,
Université Paris-Saclay CEA, CNRS,
F-91191 Gif-sur-Yvette, Cédex, France

(Dated: May 20, 2016)

Super-chameleon models where all types of matter belong to three secluded sectors, i.e. the dark, supersymmetry breaking and matter sectors, are shown to be dynamically equivalent to ultra-local models of modified gravity. In the dark sector, comprising both dark matter and dark energy, the interaction range between the dark energy field and dark matter is constrained to be extremely short, i.e. shorter than the inverse gravitino mass set by supersymmetry breaking. This realises an extreme version of chameleon screening of the dark energy interaction. On the other hand, the baryonic matter sector decouples from the dark energy in a Damour-Polyakov way. These two mechanisms preclude the existence of any modification of gravity locally in the Solar System due to the presence of the super-chameleon field. On larger scales, the super-chameleon can have effects on the growth of structure and the number of dark matter halos. It can also affect the dynamics of galaxies where the fifth force interaction that it induces can have the same order of magnitude as Newton's interaction.

PACS numbers: 98.80.-k

I. INTRODUCTION

Dark energy [1–3] is still as mysterious now as it was when the first observations of its existence appeared more than fifteen years ago. Moreover it has been realized over the last ten years that very often dark energy and a modification of gravity on large scales are intimately connected [4]. This is the case for models as diverse as $f(R)$ theories [5] or Galileons [6]. These models utilise a scalar field as the simplest way of going beyond a mere cosmological constant. Such theories where the dynamical equations of motion are of second order have been classified [7]. Their dynamics depend on the coupling of the scalar degree of freedom to matter. In the most general case [8], this coupling can be either conformal or disformal with different physical consequences. For conformal couplings, the resulting scalar-induced fifth force needs to to be screened locally. This appears to be feasible in only a few ways: chameleon [9], Damour-Polyakov [10], K-mouflage [11, 12] and Vainshtein [13]. Another mechanism, associated with the ultra-local models introduced in a companion paper [14], arises from the absence of kinetic terms and the locality of the theory. We will find in this paper that this case can be related, outside the Compton wavelength, to the chameleon models with a large mass. For disformal couplings, no fifth force is present in (quasi)-static situations [15] precluding the need for a specific screening mechanism.

All these theories involve non-linearities, either in the potential or kinetic terms and as such appear as low-energy effective field theories. In particular, the issue of the structure of the radiative corrections to the bare Lagrangian is a thorny one, only alleviated in some cases by non-renormalisation theorems, e.g. for Galileons [6] or K-mouflage [16]. For this reason, and because of its radiative stability, supersymmetry might be a promising setting for dark energy models [17, 18]. In this paper, we will consider the super-chameleon models [19, 20] where the chameleon model is embedded in a supersymmetric setting. This requires the existence of three separate sectors. The dark sector where both dark matter and dark energy live. The matter sector which should include the standard model of particle physics and finally a supersymmetry breaking sector which shifts the masses of the matter superpartners compared to their standard model counterparts. The analysis of this model was already presented in [19, 20]. Here we recall the salient features and emphasize two facts. First of all, the interaction between dark matter particles mediated by dark energy is of extremely short range, shorter than the inverse gravitino mass. Nevertheless, dark matter will see its dynamics modified, i.e. a modification of gravity, on very large scales where collective phenomena for the coarse-grained dark matter fluid can be present. Second, we also recall that ordinary matter decouples from dark energy due to the Damour-Polyakov mechanism leading to no modification of gravity in the Solar System.

In this paper we point out that on cosmological and astrophysical scales these super-chameleon models can be identified to the ultra-local models introduced in a companion paper [14]. These ultra-local models correspond to modified source models [21] where the coupling to matter has a magnitude of order $|\ln A| \lesssim 10^{-6}$ to guarantee that the contribution of modified gravity to Newton's potential is at most of order one. Ultra-local models are such that the value of the dark energy field depends algebraically on the local dark matter density. This leads to a certain number of important properties. First, the growth of structure in the linear to quasi-linear regime has an instability at short scales which is eventually tamed by the absence of fifth forces on short distances like the Solar System. This screening mechanism

is quite different from the usual screening mechanisms encountered in other modified-gravity scenarios as it directly follows from the locality of the fifth-force interaction. The intermediate region between the very large and very small scales is not amenable to our analysis and would require numerical simulations which go beyond our analysis, although we present a thermodynamic approach to investigate the fifth-force non-linear regime. We find that the number of intermediate dark matter halos is affected by the presence of the super-chameleon. This is all the more true for galactic size and mass halos where the fifth force is of the same magnitude as Newton's force. A more complete analysis would require numerical simulations which are left for future work.

This paper is organized as follows. In section II we describe the supersymmetric chameleon models and the dark and baryonic sectors. Next, in section III we show that these models can be identified with ultra-local models introduced in a companion paper, over the scales that are relevant for cosmological purposes. We describe the background dynamics and the growth of large-scale structures in section IV, considering both linear perturbation theory and the spherical collapse dynamics. In section V we estimate the magnitude of the fifth force within spherical halos and on cluster and galaxy scales. In section VI we use a thermodynamic approach to investigate the non-linear fifth-force regime for the cosmological structures that turn non-linear at high redshift and for the cores of dark matter halos. We briefly investigate the dependence on the parameter α of our results in section VII and we conclude in section VIII.

II. SUPERSYMMETRIC CHAMELEONS

A. Super-chameleons

The nature of the dark part of the Universe, i.e. dark matter and dark energy, is still unknown. It is not ruled out that both types of dark elements belong to a secluded sector of the ultimate theory of physics describing all the interactions of the Universe. In this paper, we will use a supersymmetric setting at low energy and assume that the theory comprises three sectors with only gravitational interaction between each other. We will assume that the standard model of particles to which baryons belong is one of them. We will also add a supersymmetry breaking sector $\not{SG}$ and a dark sector comprising both the dark energy field, which will turn out to be a supersymmetric version of a chameleon dark energy model, and dark matter represented by fermions in separate superfields from the super-chameleon one. For details about supersymmetry and its relation to cosmology, see for instance [22].

Baryons are introduced in a secluded sector defined by the Kähler potential K_M and the superpotential W_M. This is the matter sector which complements the dark sector and the supersymmetry breaking one. Assuming no direct interaction between the super-chameleon Φ and matter, we take for the total Kähler potential which governs the kinetic terms of the model

$$K = K(\Phi\Phi^\dagger) + K_{\not{SG}} + K_M \tag{1}$$

and similarly for the superpotential which is responsible for the interactions between the fields

$$W = W(\Phi) + W_{\not{SG}} + W_M. \tag{2}$$

The kinetic terms for the complex scalar fields ϕ^i of the model obtained as the scalar components of the superfields Φ^i are given by

$$\mathcal{L}_{\rm kin} = -K_{i\bar{j}}\,\partial_\mu\phi^i\partial^\mu\bar{\phi}^{\bar{j}} \tag{3}$$

where we have defined

$$K_{i\bar{j}} = \frac{\partial^2 K}{\partial\Phi^i\partial\bar{\Phi}^{\bar{j}}} \equiv \partial_i\bar{\partial}_{\bar{j}}K \tag{4}$$

and its matrix inverse such that $K^{i\bar{j}}K_{k\bar{j}} = \delta^i_k$. The scalar potential obtained from the F-terms of the superfields is given by

$$V_{\rm F} = K^{i\bar{j}}\partial_i W\bar{\partial}_{\bar{j}}\bar{W}, \tag{5}$$

where $\bar{W}$ is the complex conjugate of W. This is the only term in the scalar potential when the fields are not charged under gauge groups.

We will also need to add a D-term potential to the scalar potential when some extra fields in the dark sector are charged under a gauge symmetry. We will also consider the corrections due to supergravity induced by the presence of the supersymmetry breaking sector. This will be dealt with in the corresponding sections.

B. The supersymmetric model

We consider supersymmetric models where the scalar potential and the coupling to Cold Dark Matter (CDM) arise from a particular choice of the Kähler potential for the dark energy superfield Φ which is non-canonical whilst the dark matter superfields $\Phi_\pm$ have a canonical normalisation

$$K(\Phi\Phi^\dagger) = \frac{\Lambda_1^2}{2}\left(\frac{\Phi^\dagger\Phi}{\Lambda_1^2}\right)^\gamma + \Phi_+^\dagger\Phi_+ + \Phi_-^\dagger\Phi_-. \tag{6}$$

The self-interacting part of the superpotential is

$$W = \frac{\gamma}{\sqrt{2}\omega}\left(\frac{\Phi^\omega}{\Lambda_0^{\omega-3}}\right) + \frac{1}{\sqrt{2}}\left(\frac{\Phi^\gamma}{\Lambda_2^{\gamma-3}}\right), \quad 0<\omega<\gamma, \tag{7}$$

where Φ contains a complex scalar ϕ whose modulus acts as super-chameleon and $\Phi_\pm$ are chiral superfields containing dark matter fermions $\psi_\pm$. Defining the super-chameleon field as $\phi(x) = |\phi|e^{i\theta}$ and identifying $\phi \equiv |\phi|$,

one can minimise the potential over the angular field θ and after introducing the new scales

$$\Lambda = \Lambda_2 \left(\frac{\Lambda_1}{\Lambda_2}\right)^{(\gamma-1)/2}, \quad \phi_{\rm min} = \Lambda_2 \left(\frac{\Lambda_2}{\Lambda_0}\right)^{(\omega-3)/(\gamma-\omega)}, \tag{8}$$

the scalar potential becomes

$$V_{\rm F}(\phi) = K^{\Phi\Phi^\dagger}\left|\frac{dW}{d\Phi}\right|^2 = \Lambda^4\left[1-\left(\frac{\phi_{\rm min}}{\phi}\right)^{\frac{n}{2}}\right]^2, \tag{9}$$

with

$$n = 2(\gamma-\omega) \quad \text{for} \quad n \geq 2, \quad \gamma \geq \omega+1. \tag{10}$$

When $\phi \ll \phi_{\rm min}$ equation (9) reduces to the Ratra-Peebles potential [23]

$$\phi \ll \phi_{\rm min}: \quad V_{\rm F}(\phi) \approx \Lambda^4\left(\frac{\phi_{\rm min}}{\phi}\right)^n, \tag{11}$$

which has been well studied in the context of dark energy and used to define chameleons. This is the reason why this model is called super-chameleon. At larger field values the potential has a minimum at $\phi = \phi_{\rm min}$ where $V_{\rm F}(\phi_{\rm min}) = 0$ and $dW/d\phi = 0$. Supersymmetry is therefore broken whenever $\phi \neq \phi_{\rm min}$ and restored at the minimum where the supersymmetric minimum always has a vanishing energy (this follows from the supersymmetry algebra). Then, a new mechanism must be introduced in order to have a non-vanishing cosmological constant at the minimum of the potential.

C. The Fayet-Iliopoulos mechanism

An effective cosmological constant can be implemented by introducing two new scalars $\Pi_\pm = \pi_\pm + \ldots$ with charges $\pm q$ under a local U(1) gauge symmetry in the dark sector. These have the canonical Kähler potential

$$K(\Pi_\pm) = \Pi_+^\dagger e^{2qX}\Pi_+ + \Pi_-^\dagger e^{-2qX}\Pi_-, \quad q>0, \tag{12}$$

where X is the U(1) vector multiplet containing the U(1) gauge field A_μ. They are chosen to couple to the super-chameleon via the superpotential

$$W_\pi = g'\Phi\Pi_+\Pi_- \tag{13}$$

where $g' = \mathcal{O}(1)$ is a coupling constant. This construction gives rise to new terms in the scalar potential. The first contribution is the D-term potential coming from the fact that the $\Pi_\pm$ fields are charged

$$V_{\rm D} = \frac{1}{2}\left(q\pi_+^2 - q\pi_-^2 - \xi^2\right)^2, \tag{14}$$

where we have included a Fayet-Illiopoulos term ξ^2 which will later play the role of the cosmological constant. The second part of the new scalar potential is far more complicated with the addition of these new fields but when $\langle\pi_-\rangle = 0$ it simplifies and the sum of both terms yields

$$V(\pi_+) = \frac{1}{2}\left(q\pi_+^2 - \xi^2\right)^2 + g'^2\phi^2\pi_+^2; \quad \langle\pi_-\rangle = 0, \tag{15}$$

where we have put $\pi_+ = |\pi_+|$. It can be shown [19] that $\langle\pi_-\rangle = 0$ minimises the whole potential so we only consider the effects of the new term $V(\pi_+)$. In particular, the mass of the charged scalar π_+ is

$$m_{\pi_+}^2 = 2g'^2\phi^2 - 2q\xi^2. \tag{16}$$

At early times the super-chameleon is small ($\phi \ll \phi_{\rm min}$) and this mass is negative. The U(1) symmetry is therefore broken ($\langle\pi_+\rangle \neq 0$). However, as the cosmological field evolves towards its minimum this mass increases until it reaches zero, restoring the symmetry so that $\langle\pi_+\rangle = 0$. Minimising (15) with respect to π_+ one finds

$$\phi < \frac{\sqrt{q}}{g'}\xi: \quad V_{\rm min} = -\frac{m_{\pi_+}^4}{8q^2} + \frac{\xi^4}{2}, \tag{17}$$

$$\phi > \frac{\sqrt{q}}{g'}\xi: \quad V_{\rm min} = \frac{\xi^4}{2}. \tag{18}$$

Therefore, at late times we recover the present-day dark energy density by taking

$$\xi^4 = 2\bar{\rho}_{\rm de0}, \tag{19}$$

which gives $\xi \sim 10^{-3}$eV. This mechanism requires that $\phi_{\rm min} > \sqrt{q}\xi/g'$, which imposes restrictions on the parameter space,

$$\Lambda_2\left(\frac{\Lambda_2}{\Lambda_0}\right)^{(\omega-3)/(\gamma-\omega)} > \frac{\sqrt{q}}{g'}\left(2\bar{\rho}_{\rm de0}\right)^{1/4}. \tag{20}$$

D. The coupling to Cold Dark Matter

Dark energy in the form of Φ is coupled to dark matter. The coupling function between the two dark sides of the model is found by considering the interaction of Φ and $\Phi_\pm$

$$W_{\rm int} = m\left[1 + \frac{g\,\Phi^\sigma}{m\,\Lambda_3^{\sigma-1}}\right]\Phi_+\Phi_-, \quad \sigma>0, \tag{21}$$

which gives a super-chameleon dependent mass to the dark matter fermions

$$\mathcal{L} \supset \frac{\partial^2 W_{\rm int}}{\partial\Phi_+\partial\Phi_-}\psi_+\psi_-. \tag{22}$$

When the dark matter condenses to a finite density, $\rho = m\langle\psi_+\psi_-\rangle$, this term gives a density-dependent contribution to the scalar potential

$$\mathcal{L} \supset A(\phi)\rho, \tag{23}$$

from which one can read off the coupling function

$$A(\phi) = 1 + \frac{g\,\phi^\sigma}{m\,\Lambda_3^{\sigma-1}}. \tag{24}$$

This function reappears in the form of the conformal coupling between dark matter and dark energy considered as a scalar-tensor theory

E. The normalised dark-energy scalar field φ

Because $K_{\phi\bar\phi} \neq 1$ the field ϕ is not canonically normalised, since the kinetic term in the Lagrangian reads

$$\mathcal{L}_{\rm kin} = -K_{\phi\bar\phi}\,\partial_\mu\phi\partial^\mu\bar\phi = -\frac{\gamma^2}{2}\left(\frac{|\phi|}{\Lambda_1}\right)^{2(\gamma-1)}\partial_\mu\phi\partial^\mu\bar\phi. \tag{25}$$

The normalised field is then easily defined by

$$\varphi = \Lambda_1\left(\frac{\phi}{\Lambda_1}\right)^\gamma, \tag{26}$$

and the coupling function (24) becomes

$$A(\varphi) = 1 + \alpha\left(\frac{\varphi}{\varphi_{\rm min}}\right)^{\sigma/\gamma} \quad \text{with} \quad \alpha \equiv \frac{g\phi_{\rm min}^\sigma}{m\Lambda_3^{\sigma-1}}, \tag{27}$$

and

$$\varphi_{\rm min} = \Lambda_1\left(\frac{\phi_{\rm min}}{\Lambda_1}\right)^\gamma = \Lambda_1\left(\frac{\Lambda_2}{\Lambda_1}\right)^\gamma\left(\frac{\Lambda_2}{\Lambda_0}\right)^{\gamma(\omega-3)/(\gamma-\omega)}, \tag{28}$$

while the effective potential $V_{\rm F}(\varphi) + \rho(A(\varphi)-1)$ is

$$V_{\rm eff}(\varphi) = \Lambda^4\left[\left(\frac{\varphi_{\rm min}}{\varphi}\right)^{n/2\gamma} - 1\right]^2 + \alpha\,\rho\left(\frac{\varphi}{\varphi_{\rm min}}\right)^{\sigma/\gamma}. \tag{29}$$

Notice that the effective potential in this model coincides with the one obtained in a scalar tensor theory with the potential $V_{\rm F}(\varphi)$ and the coupling function $A(\varphi)$. We will exploit this fact below. Since we require the cosmology to remain close to the Λ-CDM scenario, i.e. the fifth force must not be much greater than Newtonian gravity, within this framework we can infer that the coupling function $A(\varphi)$ must remain close to unity. This provides the constraint

$$\alpha \ll 1 \tag{30}$$

on the parameter combination α of Eq.(27).

The dynamics of the model can be determined by minimizing the effective potential. This leads to the minimum φ of the theory in the presence of matter (CDM)

$$\left(\frac{\varphi_{\rm min}}{\varphi}\right)^{(n+\sigma)/\gamma} - \left(\frac{\varphi_{\rm min}}{\varphi}\right)^{(n+2\sigma)/2\gamma} = \frac{\rho}{\rho_\infty}, \tag{31}$$

where we have defined the energy density

$$\rho_\infty = \frac{n}{\alpha\sigma}\Lambda^4 = \bar\rho_0(1+z_\infty)^3, \quad \text{and} \quad 0 < \varphi \leq \varphi_{\rm min}\,, \tag{32}$$

where z_∞ is the redshift below which the field becomes close to its supersymmetric minimum $\varphi_{\rm min}$[34].

As in scalar tensor theories, such as dilaton models or $f(R)$ theories, it is convenient to introduce the coupling $\beta(\varphi)$ defined by

$$\beta(\varphi) = M_{\rm Pl}\frac{d\ln A}{d\varphi} \tag{33}$$

$$= \frac{\alpha\sigma}{\gamma}\frac{M_{\rm Pl}}{\varphi_{\rm min}}\left[1 + \alpha\left(\frac{\varphi}{\varphi_{\rm min}}\right)^{\sigma/\gamma}\right]^{-1}\left(\frac{\varphi}{\varphi_{\rm min}}\right)^{\sigma/\gamma-1} \tag{34}$$

and the effective mass $m_{\rm eff}^2 = \partial^2 V_{\rm eff}/\partial\varphi^2$ at the minimum of the effective potential,

$$m_{\rm eff}^2(\varphi) = \frac{\alpha\sigma}{\gamma}\frac{\rho_\infty}{\varphi^2}\left(\frac{\varphi}{\varphi_{\rm min}}\right)^{\sigma/\gamma}\left[\frac{n}{\gamma}\left(\frac{\varphi_{\rm min}}{\varphi}\right)^{(n+\sigma)/\gamma} - \frac{n}{2\gamma}\left(\frac{\varphi_{\rm min}}{\varphi}\right)^{(n+2\sigma)/2\gamma} + \frac{\sigma}{\gamma}\frac{\rho}{\rho_\infty}\right], \tag{35}$$

where we used Eq.(31). The quasi-static approximation (32) applies if $m_{\rm eff}^2 \gg H^2$. This holds for redshifts $z \leq z_\infty$ provided

$$\frac{\alpha\rho_\infty}{\varphi_{\rm min}^2} \gg H_\infty^2, \quad \text{whence} \quad \left(\frac{\varphi_{\rm min}}{M_{\rm Pl}}\right)^2 \ll \alpha, \tag{36}$$

where in the second inequality we assumed $z_\infty \leq z_{\rm eq}$. At higher redshifts, $m_{\rm eff}(z)$ grows at least as fast as $H(z)$ in both the matter and radiation eras if we have

$$\text{matter era: } \sigma \leq 2\gamma, \ \text{ radiation era: } \sigma \leq \gamma + \omega/2. \tag{37}$$

F. Supersymmetry breaking

Supersymmetry is broken by values much larger than the energy density of CDM. This is achieved in a dedicated sector of the theory which we do not need to specify here. Gravitational interactions lead to a correction to the scalar potential coming from supersymmetry breaking [20]

$$\Delta V_{\not SG} = \frac{m_{3/2}^2\,|K_\Phi|^2}{K_{\Phi\Phi^\dagger}} \sim \frac{m_{3/2}^2\phi^{2\gamma}}{\Lambda_1^{2\gamma-2}}, \tag{38}$$

where $m_{3/2}$ is the gravitino mass. This competes with the density dependent term in the effective potential (29). This correction does not upset the dynamics of the model as long as

$$\left(\frac{\varphi_{\rm min}}{M_{\rm Pl}}\right)^2 \ll \frac{\alpha\rho_\infty}{M_{\rm Pl}^2 m_{3/2}^2}. \tag{39}$$

This is typically much more stringent than the quasi-static condition (36). Using Eq.(35) this can also be shown to correspond to a condition on the mass of the scalar field φ at the supersymmetric minimum, for $z \leq z_\infty$,

$$m^2_{\rm eff}(\varphi_{\rm min}) \sim \frac{\alpha\rho_\infty}{\varphi^2_{\rm min}} \gg m^2_{3/2}. \tag{40}$$

As the gravitino mass is always greater than 10^{-5} eV in realistic models of supersymmetry breaking [24], we deduce that the range of the scalar interaction mediated by φ is very small, at most at the cm level. Because the scalar interaction has such a short range, we call these models ultra-local. In fact, we shall see below that they can be related to the so-called"ultra-local models" introduced in the companion paper [14].

G. Coupling to baryons

We consider that matter fermions ψ belong to a superfield Φ_M. The mass of the canonically normalised matter fermions becomes

$$m_\psi = e^{K(\Phi,\Phi^\dagger)/2M^2_{\rm Pl}}\, m^{(0)}_\psi, \tag{41}$$

where $m^{(0)}_\psi$ is the bare mass of the baryons $\frac{\partial^2 W}{\partial\Phi^2_M}$. The exponential prefactor is at the origin of the coupling function between the matter fields and the super-chameleon in the Einstein frame. This leads to the identification of coupling function in the matter sector

$$A_M(\varphi) = e^{\varphi^2/2M^2_{\rm Pl}} \tag{42}$$

for the canonically normalised super-chameleon, and the coupling to baryons

$$\beta_M(\varphi) = \frac{\varphi}{M_{\rm Pl}}, \tag{43}$$

which is the coupling of a dilaton to matter. As long as $\varphi_{\rm min} \ll M_{\rm Pl}$, which is already required to suppress the supergravity corrections to the scalar potential, the coupling to baryons is negligible. Hence this model describes a scenario where dark energy essentially couples to dark matter and decouples from ordinary matter.

III. THE SUPERSYMMETRIC CHAMELEON AS AN ULTRA-LOCAL MODEL

A. Definition of ultra-local models

We define ultra-local scalar field models by the action [14]

$$\begin{aligned} S \;=\; & \int d^4x\,\sqrt{-\tilde g}\left[\frac{\tilde M^2_{\rm Pl}}{2}\tilde R + \tilde{\mathcal L}_\varphi(\varphi)\right] \\ & + \int d^4x\,\sqrt{-g}\,\mathcal L_{\rm m}(\psi^{(i)}_{\rm m}, g_{\mu\nu}), \end{aligned} \tag{44}$$

where the dark matter fields $\psi^{(i)}_{\rm m}$ follow the Jordan-frame metric $g_{\mu\nu}$, with determinant g, which is related to the Einstein-frame metric $\tilde g_{\mu\nu}$ by

$$g_{\mu\nu} = A^2(\varphi)\tilde g_{\mu\nu}. \tag{45}$$

We explicitly take no coupling between baryons and the scalar field to make possible the equivalence with the supersymmetric chameleon models. In this paper we restrict ourselves to large cosmological scales, which are dominated by the dark matter, and we neglect the impact of baryons. Ultra-local models are defined by the property that their scalar-field kinetic term is negligible,

$$\tilde{\mathcal L}_\varphi(\varphi) = -V(\varphi). \tag{46}$$

Introducing the characteristic energy scale $\mathcal M^4$ of the potential and the dimensionless field $\tilde\chi$ as

$$\tilde\chi \equiv -\frac{V(\varphi)}{\mathcal M^4}, \quad \text{and} \quad A(\tilde\chi) \equiv A(\varphi), \tag{47}$$

these models are fully specified by a single function, $A(\tilde\chi)$, which is defined from the initial potential $V(\varphi)$ and coupling function $A(\varphi)$ through Eq.(47). In other words, because the kinetic term is negligible there appears a degeneracy between the potential $V(\varphi)$ and the coupling function $A(\varphi)$. The change of variable (47) absorbs this degeneracy and we are left with a single free function $A(\tilde\chi)$.

B. Cosmological background of ultra-local models

Because the matter fields follow the geodesics set by the Jordan frame and satisfy the usual conservation equations in this frame, we mostly work in the Jordan frame. We introduce the time dependent coupling

$$\epsilon_2(t) \equiv \frac{d\ln\bar A}{d\ln a}, \tag{48}$$

such that, as shown in the companion paper, the Friedmann equation reads as

$$3M^2_{\rm Pl}\mathcal H^2 = (1-\epsilon_2)^{-2}a^2(\bar\rho + \bar\rho_{\rm rad} + \bar\rho_{\tilde\chi}), \tag{49}$$

where τ is the conformal time, $\mathcal H$ the conformal Hubble expansion rate, and the Jordan-frame Planck mass is

$$M^2_{\rm Pl}(t) = \bar A^{-2}(t)\,\tilde M^2_{\rm Pl}, \tag{50}$$

while $\bar\rho$, $\bar\rho_{\rm rad}$ and $\bar\rho_{\tilde\chi}$ are the matter, radiation and scalar field energy densities. In particular, the background matter and radiation densities evolve as usual as

$$\bar\rho = \frac{\bar\rho_0}{a^3}, \quad \bar\rho_{\rm rad} = \frac{\bar\rho_{\rm rad0}}{a^4}, \tag{51}$$

while the scalar field energy density is given by

$$\bar\rho_{\tilde\chi} = -\bar A^{-4}\mathcal M^4\bar{\tilde\chi}, \tag{52}$$

and the equation of motion of the background scalar field is

$$\mathcal{M}^4 = \bar{A}^4\bar{\rho}\frac{d\ln\bar{A}}{d\bar{\tilde{\chi}}} \quad \text{hence} \quad \frac{d\bar{\tilde{\chi}}}{d\tau} = \bar{A}^4\frac{\bar{\rho}}{\mathcal{M}^4}\epsilon_2\mathcal{H}. \tag{53}$$

It is convenient to write the Friedmann equation (49) in a more standard form by introducing the effective dark energy density $\bar{\rho}_{\rm de}$ defined by

$$3M_{\rm Pl}^2\mathcal{H}^2 = a^2(\bar{\rho} + \bar{\rho}_{\rm rad} + \bar{\rho}_{\rm de}), \tag{54}$$

which gives

$$\bar{\rho}_{\rm de} = \bar{\rho}_{\tilde{\chi}} + \frac{2\epsilon_2 - \epsilon_2^2}{(1-\epsilon_2)^2}(\bar{\rho} + \bar{\rho}_{\rm rad} + \bar{\rho}_{\tilde{\chi}}). \tag{55}$$

C. Cosmological perturbations of ultra-local models

We write the Newtonian gauge metric as

$$ds^2 = a^2[-(1+2\Phi)d\tau^2 + (1-2\Psi)d\mathbf{x}^2], \tag{56}$$

so that the Einstein- and Jordan-frame metric potentials are related by

$$1+2\Phi = \frac{A^2}{\bar{A}^2}(1+2\tilde{\Phi}), \quad 1-2\Psi = \frac{A^2}{\bar{A}^2}(1-2\tilde{\Psi}), \tag{57}$$

while the Jordan-frame Newtonian potential is defined by

$$\frac{\nabla^2}{a^2}\Psi_{\rm N} \equiv \frac{\delta\rho + \delta\rho_{\tilde{\chi}}}{2M_{\rm Pl}^2}. \tag{58}$$

Because we wish the deviations of Φ and Ψ from the Newtonian potential $\Psi_{\rm N}$ to remain modest, and we typically have $|\Psi_{\rm N}| \lesssim 10^{-5}$ for cosmological and astrophysical structures, we require $|\delta\ln A| \lesssim 10^{-5}$ and $|\delta\rho_{\tilde{\chi}}| \lesssim |\delta\rho|$. This first constraint is fulfilled by choosing coupling functions $A(\tilde{\chi})$ that are bounded and deviate from unity by less than 10^{-5}, which reads as

$$|\ln A(\tilde{\chi})| \lesssim 10^{-5}, \tag{59}$$

while the second constraint will follow naturally because the characteristic scalar field energy density is the dark energy density today. Then, we can linearize Eq.(57) in $\delta\ln A$. This leads to

$$\Phi = \Psi_{\rm N} + \delta\ln A, \quad \Psi = \Psi_{\rm N} - \delta\ln A, \tag{60}$$

while the dark energy density fluctuations read as

$$\delta\rho_{\tilde{\chi}} = -\mathcal{M}^4\delta\tilde{\chi}. \tag{61}$$

In Eq.(61) and in the following we use the characteristic property (59) of ultra-local models to write $A \simeq 1$ wherever this approximation is valid within a 10^{-5} accuracy (the only place where deviations of A from unity are important is for the computation of the fifth force through the gradient $\nabla\ln A$).

In general configurations including perturbations, the equation of motion of the scalar field reads as

$$\frac{d\ln A}{d\tilde{\chi}} = \frac{\mathcal{M}^4}{\rho}. \tag{62}$$

The dark matter component obeys the continuity and Euler equations

$$\frac{\partial\rho}{\partial\tau} + (\mathbf{v}\cdot\nabla)\rho + (3\mathcal{H} + \nabla\cdot\mathbf{v})\rho = 0, \tag{63}$$

and

$$\frac{\partial\mathbf{v}}{\partial\tau} + (\mathbf{v}\cdot\nabla)\mathbf{v} + \mathcal{H}\mathbf{v} = -\nabla\Phi. \tag{64}$$

From Eq.(60) we have $\nabla\Phi = \nabla\Psi_{\rm N} + \nabla\ln A$, and then the scalar field equation (62) gives

$$\nabla\ln A = \frac{\mathcal{M}^4}{\rho}\nabla\tilde{\chi}. \tag{65}$$

Thus in terms of matter dynamics, the scalar field appears via the modification of the Poisson equation (58), because of the additional source associated to the scalar field and the time dependent Planck mass, and via the appearance of the "new" term (65) in the Euler equation (64), which is due to the spatial variation of $\ln A$.

On large scales we may linearize the equations of motion. Expanding the coupling function $A(\tilde{\chi})$ as

$$\ln A(\tilde{\chi}) = \ln\bar{A} + \sum_{n=1}^{\infty}\frac{\beta_n(t)}{n!}(\delta\tilde{\chi})^n, \tag{66}$$

the scalar field equation (62) gives at the background and linear orders

$$\beta_1 = \frac{\mathcal{M}^4}{\bar{\rho}}, \quad \delta\tilde{\chi} = -\frac{\beta_1}{\beta_2}\delta. \tag{67}$$

Defining

$$\epsilon_1(t) \equiv \frac{\beta_1}{\beta_2}\frac{\mathcal{M}^4}{\bar{\rho}} = \frac{\beta_1^2}{\beta_2}, \tag{68}$$

we have for the linear matter density contrast δ

$$\frac{\partial\delta^2}{\partial\tau^2} + \mathcal{H}\frac{\partial\delta}{\partial\tau} + \epsilon_1 c^2\nabla^2\delta = \frac{\bar{\rho}a^2}{2M_{\rm Pl}^2}(1+\epsilon_1)\delta, \tag{69}$$

which also reads in Fourier space as

$$\frac{\partial^2\delta}{\partial\tau^2} + \mathcal{H}\frac{\partial\delta}{\partial\tau} - \frac{3}{2}\Omega_{\rm m}(\tau)\mathcal{H}^2\left[1+\epsilon(k,\tau)\right]\delta = 0, \tag{70}$$

where $\epsilon(k,\tau)$, which corresponds to the deviation from the Λ-CDM cosmology, is given by

$$\epsilon(k,\tau) = \epsilon_1(\tau)\left[1 + \frac{2}{3\Omega_{\rm m}}\frac{c^2k^2}{a^2H^2}\right]. \tag{71}$$

The k-dependent term dominates when $ck/aH > 1$, i.e. on sub-horizon scales. Moreover, we have $(ck/aH)^2 \sim 10^7$ today at scales of about $1\,h^{-1}$Mpc. Therefore, we must have

$$|\epsilon_1| \lesssim 10^{-7} \tag{72}$$

to ensure that the growth of large-scale structures is not too significantly modified. This small value does not require introducing additional small parameters as it will follow from the constraint (59), which already leads to the introduction of a small parameter $\alpha \lesssim 10^{-5}$ that gives the amplitude of the coupling function $\ln A$.

The quantity ϵ_2 introduced in Eq.(48) is related to the quantity ϵ_1 defined in Eq.(68) by

$$\epsilon_2 = 3\epsilon_1, \;\; \text{hence} \;\; |\epsilon_2| \lesssim 10^{-7}. \tag{73}$$

This implies that at the background level the ultra-local model behaves like the Λ-CDM cosmology, see Eqs.(52)-(55), as the scalar field and dark energy densities coincide and are almost constant at low z, within an accuracy of 10^{-6}.

D. Super-chameleon identification

Super-chameleon models are such that the mass of the scalar field is so large that the kinetic terms are negligible. They behave like ultra-local models on distances $r \gtrsim m_{\rm eff}^{-1}$. It is only on very short distances, which are negligible on astrophysical and cosmological scales, that the kinetic terms play a role. The identification with an ultra-local model is therefore valid on scales

$$\frac{k}{a} \lesssim m_{\rm eff}; \quad \text{this includes the range } \; \frac{k}{a} \lesssim m_{3/2} \ll m_{\rm eff}, \tag{74}$$

where we used Eq.(40). Even as early as $a_{\rm BBN} \sim 10^{-10}$, the model is equivalent to an ultra-local model on comoving scales larger than 10 km, well below the distances of interest in the growth of cosmological structures. As a result, for all practical purposes super-chameleon models can be identified with ultra-local models. Thus, the coupling function $A(\varphi)$ and the potential $V(\varphi)$ defined in Eqs.(45)-(46) for the ultra-local model can be read from the effective potential (29) of the super-chameleon model, to which we must add the cosmological constant contribution (18). Using the mapping (47) in terms of the dimensionless field $\tilde\chi$ this yields

$$A(\tilde\chi) = 1 + \alpha \left(\frac{\varphi}{\varphi_{\rm min}}\right)^{\sigma/\gamma} \tag{75}$$

and

$$-\mathcal{M}^4\tilde\chi = V = \Lambda^4 \left[\left(\frac{\varphi_{\rm min}}{\varphi}\right)^{n/2\gamma} - 1\right]^2 + \frac{\xi^4}{2}. \tag{76}$$

We have seen in Eq.(19) that $\xi^4 = 2\bar\rho_{\rm de0}$ to recover the cosmological constant associated with the current expansion of the Universe. We can also take $\mathcal{M}^4 = \bar\rho_{\rm de0}$ without loss of generality, as this only sets the choice of normalization of $\tilde\chi$. To simplify the model we also take $\Lambda^4 = \bar\rho_{\rm de0}$, which avoids introducing another scale. This gives

$$\mathcal{M}^4 = \Lambda^4 = \bar\rho_{\rm de0}: \quad \tilde\chi = -1 - \left[\left(\frac{\varphi_{\rm min}}{\varphi}\right)^{n/2\gamma} - 1\right]^2 \tag{77}$$

and

$$A(\tilde\chi) = 1 + \alpha \left(1 + \sqrt{-1-\tilde\chi}\right)^{-2\sigma/n} \;\; \text{with} \;\; \tilde\chi \le -1, \tag{78}$$

which is the expression of the coupling function in terms of the ultra local scalar field. The comparison with the supersymmetric model can be completed by verifying that the cosmological perturbations also obey the same dynamics.

The coupling of dark energy to dark matter implies that the growth of the density contrast of CDM is modified [25–27] and the linear density contrast $\delta = \delta\rho/\rho$ of the super-chameleon model in the conformal Newtonian Gauge evolves on sub-horizon scales according to

$$\frac{\partial\delta}{\partial\tau^2} + \mathcal{H}\frac{\partial\delta}{\partial\tau} - \frac{3}{2}\Omega_{\rm m}(\tau)\mathcal{H}^2 \left(1 + \frac{2\beta^2(\varphi)}{1 + \frac{m_{\rm eff}^2 a^2}{k^2}}\right)\delta = 0. \tag{79}$$

Physically, the last term in (79) corresponds to a scale dependent enhancement of Newton's constant. As the mass of the scalar field is always very large compared to astrophysical wave numbers, we can simplify (79) to find

$$\frac{\partial\delta}{\partial\tau^2} + \mathcal{H}\frac{\partial\delta}{\partial\tau} - \frac{3}{2}\Omega_{\rm m}(\tau)\mathcal{H}^2 \left(1 + \frac{2k^2\beta^2(\varphi)}{m_{\rm eff}^2 a^2}\right)\delta = 0 \tag{80}$$

for $k/a \ll m_{\rm eff}$. This equation is the same as the equation (70) obtained for the ultra-local models, on sub-horizon scales where we can neglect the unit factor in Eq.(71). Indeed, the chameleon coupling $\beta(\varphi)$ defined in Eq.(33), $\beta = M_{\rm Pl} d\ln A/d\varphi$, and the ultra-local coupling $\beta_1(\tilde\chi)$ defined in Eq.(66), $\beta_1 = d\ln A/d\tilde\chi$, are related by

$$\beta = \beta_1 M_{\rm Pl}\frac{d\tilde\chi}{d\varphi}. \tag{81}$$

From the identification (76) we can write the effective chameleon potential of Eq.(29) as

$$V_{\rm eff}(\varphi) = -\mathcal{M}^4\tilde\chi + \rho(A-1) - \bar\rho_{\rm de0}, \tag{82}$$

where we explicitly subtract the cosmological constant. Then, the quasi-static equation (31) for φ, which corresponds to the minimum of the potential $\partial V_{\rm eff}/\partial\varphi = 0$, yields $\beta_1 = \mathcal{M}^4/\rho$, where we used Eq.(81) and $A \simeq 1$, and we recover the ultra-local equation of motion (62)-(67). Next, from the definition of the chameleon effective

mass, $m^2_{\rm eff} = \partial^2 V_{\rm eff}/\partial\varphi^2$, we obtain using Eq.(82) and the result $\beta_1 = \mathcal{M}^4/\rho$,

$$m^2_{\rm eff}(\varphi) = \frac{\rho\beta_2\beta^2}{M^2_{\rm Pl}\beta_1^2}, \tag{83}$$

where the ultra-local factor $\beta_2 = d^2 \ln A/d\tilde{\chi}^2 = d\beta_1/d\tilde{\chi}$ was introduced in Eq.(66). This gives $2\beta^2/m^2_{\rm eff} = 2M^2_{\rm Pl}\beta_1^2/\rho\beta_2$ and we find that Eq.(80) coincides with Eq.(70) over the range $H \ll k/a \ll m_{\rm eff}$, using the second expression (68) for $\epsilon_1(t)$.

This identification of the super-chameleon model with the ultra-local model shows that on cosmological scales, $H \ll k/a \ll m_{\rm eff}$, the dynamics is set by the single function $A(\tilde{\chi})$ obtained in Eq.(78). This implies that structure formation is only sensitive to two combinations of the parameters introduced in the supersymmetric chameleon setting, namely the exponent ratio σ/n and the ratio $\Lambda^4/\bar{\rho}_{\rm de0}$ (which we set to unity in this paper), in addition to the cosmological constant $\xi^4/2 = \bar{\rho}_{\rm de0}$. Conversely, there is a wide model degeneracy and the same coupling function (78) corresponds to many different chameleon models.

We can note here that in the context of usual chameleon models such as $f(R)$ theories, where $\beta \sim 1$, having a very large effective mass $m^2_{\rm eff}$, with $m^{-1}_{\rm eff} \ll 10^{-4}$mm, would lead to negligible departure from the Λ-CDM cosmology for the formation of large scale structures, as seen from Eq.(80). This is not the case for the super-chameleon models studied in this paper because the coupling β is also very large and much greater than unity. Indeed, from Eq.(34) we have $\beta \sim \alpha M_{\rm Pl}/\varphi_{\rm min} \gg 1$, whereas from Eq.(35) we have $m^2_{\rm eff} \sim \alpha\rho_\infty/\varphi^2_{\rm min}$. This yields

$$\frac{\beta^2}{m^2_{\rm eff}} \sim \frac{\alpha^2 M^2_{\rm Pl}}{\Lambda^4}, \tag{84}$$

and $\beta^2 k^2/m^2_{\rm eff}a^2$ can be of order unity on kpc to Mpc scales, even with $\alpha \ll 1$, as we typically have $\Lambda^4 \sim M^2_{\rm Pl}H_0^2$.

E. Example of models

It is interesting to consider templates for ultra-local models coming from super-chameleons.

A good set of models can be obtained for instance by taking the cut-off of the theory $\Lambda_1 = M_{\rm Pl}$ in the Kähler potential (6). To obtain $\Lambda^4 = \bar{\rho}_{\rm de0}$ as in Eq.(77) this requires the non-renormalised scale in the superpotential W of Eq.(7) to be $\Lambda_2 = M_{\rm Pl}(\bar{\rho}_{\rm de0}/M^4_{\rm Pl})^{1/(6-2\gamma)}$. A simple choice for the exponents ω and γ is $\omega = 1$ and $\gamma = 2$, which gives $n = 2$ and the Kähler potential becomes

$$K(\Phi\Phi^\dagger) = \frac{M^2_{\rm Pl}}{2}\left(\frac{\Phi^\dagger\Phi}{M^2_{\rm Pl}}\right)^2 + \Phi_+^\dagger\Phi_+ + \Phi_-^\dagger\Phi_- \tag{85}$$

while the self-interacting part of the superpotential is

$$W = \sqrt{2}\Lambda_0^2\Phi + \sqrt{\frac{3\Omega_{\rm de0}}{2}}H_0\Phi^2, \tag{86}$$

which contains a linear term and a mass term, with $\Lambda_2 = \sqrt{3\Omega_{\rm de0}}H_0$. Both Λ_0 and H_0 are protected by supersymmetry under renormalisation.

The supersymmetric minimum $\phi_{\rm min}$ of Eq.(8) becomes

$$\phi_{\rm min} = \frac{\Lambda_0^2}{\Lambda_2}. \tag{87}$$

Requiring that $\phi_{\rm min} > \sqrt{q}\xi/g'$ to recover the late cosmological constant behavior (18) and using Eq.(19) we obtain the lower bound on Λ_0

$$\Lambda_0^2 \gtrsim M^2_{\rm Pl}\left(\frac{H_0}{M_{\rm Pl}}\right)^{3/2}. \tag{88}$$

The normalized chameleon field φ of Eq.(26) reads as

$$\frac{\varphi}{M_{\rm Pl}} = \frac{\phi^2}{M^2_{\rm Pl}}, \qquad \frac{\varphi_{\rm min}}{M_{\rm Pl}} = \frac{\Lambda_0^4}{3\Omega_{\rm de0}M^2_{\rm Pl}H_0^2}, \tag{89}$$

while the characteristic density ρ_∞ of Eq.(32) is

$$\rho_\infty = \frac{2}{\alpha\sigma}\bar{\rho}_{\rm de0} \sim \frac{\bar{\rho}_{\rm de0}}{\alpha}. \tag{90}$$

We must also satisfy the constraint (39), which yields the upper bound on Λ_0

$$\Lambda_0^2 \ll M^2_{\rm Pl}\left(\frac{H_0}{M_{\rm Pl}}\right)^{3/2}\left(\frac{M_{\rm Pl}}{m_{3/2}}\right)^{1/2}. \tag{91}$$

As we always have $m_{3/2} \ll M_{\rm Pl}$, the comparison of Eq.(91) with Eq.(88) shows that the range of values for Λ_0 is fairly large.

The scales m and Λ_3 of the dark matter interaction $W_{\rm int}$ in Eq.(21) are only constrained through their combination with $\phi_{\rm min}$ in the coupling parameter α of Eq.(27), which must be small as noticed in Eq.(30). In fact, the identification with the ultra-local model and the study presented in the companion paper shows that we must require $\alpha \lesssim 10^{-6}$ to keep the formation of large cosmological structures close to the Λ-CDM behavior. From Eq.(37) the exponent σ should satisfy $\sigma \leq 5/2$ if we wish to ensure that the quasi-static approximation remains valid up to arbitrarily high redshifts, which gives $0 < \sigma/n \leq 5/4$. More generally, combining Eqs.(10) and (37) we have

$$0 < \frac{\sigma}{n} \leq \frac{\gamma + \omega/2}{2(\gamma - \omega)} \quad \text{hence} \quad 0 < \frac{\sigma}{n} \leq \frac{3\gamma - 1}{4}. \tag{92}$$

It is interesting to obtain the characteristic scales of the coupling β and effective mass $m_{\rm eff}$ of these super-chameleon models. Using the bounds (88) and (91) we obtain

$$\beta \sim \frac{\alpha M^2_{\rm Pl}H_0^2}{\Lambda_0^4} \quad \text{hence} \quad \frac{\alpha m_{3/2}}{H_0} \ll \beta \lesssim \frac{\alpha M_{\rm Pl}}{H_0}, \tag{93}$$

and

$$m_{\rm eff}^2 \sim \frac{M_{\rm Pl}^4 H_0^5}{\Lambda_0^8} \quad \text{hence} \quad m_{3/2}^2 \ll m_{\rm eff}^2 \lesssim M_{\rm Pl}^2. \qquad (94)$$

We can check that both β and $m_{\rm eff}$ are large in these super-chameleon models.

As noticed above from Eq.(78), eventually we will study the super-chameleon models of this type where the only parameters are α, which will be chosen to be 10^{-6} or lower, and $\zeta = \sigma/n$, of order unity.

IV. ULTRA-LOCAL DYNAMICS

A. Chameleon and ultra-local potentials and coupling functions

As the total variation of $A(\tilde\chi)$ is bounded by $\alpha \lesssim 10^{-6}$, we can approximate Eq.(78) as

$$\ln A(\tilde\chi) = \alpha \left(1 + \sqrt{-1-\tilde\chi}\right)^{-2\zeta}, \quad \zeta > 0, \qquad (95)$$

where we defined $\zeta = \sigma/n$. Equation (95) fully defines the ultra-local model that corresponds to the super-chameleon models considered in this paper. For the numerical applications below we take $\alpha = 10^{-6}$ and ζ among $\{1/2, 1, 3/2\}$. The first two choices can be obtained with $\sigma = 1$ and $\sigma = 2$ for the explicit super-chameleon model described in section III E with $\gamma = n = 2$. The choice $\zeta = 3/2$ requires a model with $\gamma \geq 7/3$ or corresponds to a model with $\gamma < 7/3$ where the field φ has not yet reached the quasi-static equilibrium (31) at very high redshift (which is not very important as the dark energy and the fifth force do not play a significant role at high redshifts far in the radiation era).

Using Eq.(95), the equation for the evolution of the scalar field (62) becomes

$$\frac{\rho}{\rho_\alpha} = \frac{1}{\zeta}\sqrt{-1-\tilde\chi}\left(1 + \sqrt{-1-\tilde\chi}\right)^{2\zeta+1}, \qquad (96)$$

where we introduced

$$\rho_\alpha = \frac{\mathcal{M}^4}{\alpha} = \frac{\bar\rho_{\rm de0}}{\alpha}. \qquad (97)$$

This explicitly shows that, because of the small parameter α, such models introduce a second density scale $\rho_\alpha \gtrsim 10^6 \bar\rho_{\rm de0}$ in addition to the current dark energy density $\bar\rho_{\rm de0}$.

Eq.(96) can be used to express $\tilde\chi$ as a function of the density in the high- and low-density limits,

$$\rho \gg \rho_\alpha : \quad \tilde\chi(\rho) \sim -\left(\frac{\zeta\rho}{\rho_\alpha}\right)^{1/(1+\zeta)}, \qquad (98)$$

$$\rho \ll \rho_\alpha : \quad \tilde\chi(\rho) \simeq -1 - \left(\frac{\zeta\rho}{\rho_\alpha}\right)^{2}. \qquad (99)$$

At the background level, we switch from the high-density regime (98) to the low-density regime (99) at the redshift z_α, with

$$a_\alpha = \alpha^{1/3} \lesssim 0.01, \quad z_\alpha = \alpha^{-1/3} \gtrsim 100, \quad \bar\rho(z_\alpha) = \rho_\alpha. \qquad (100)$$

Thus, together with the density scale ρ_α these ultra-local models also select a particular redshift $z_\alpha \gtrsim 100$. This is the redshift where the fifth force effects are the strongest, in terms of the formation of cosmological structures, even though at the background level the scalar field energy density only becomes dominant at low z as a dark energy contribution. Up to factors of order unity, the density ρ_α and redshift z_α also correspond to the density ρ_∞ and redshift z_∞ introduced in Eq.(32), where the super-chameleon field φ reaches the supersymmetric minimum $\varphi_{\rm min}$ (we chose $\Lambda^4 = \bar\rho_{\rm de0}$). Thus, within this supersymmetric setting the density and redshift (ρ_α, z_α) obtain an additional physical meaning.

From Eqs.(98) and (99) we also obtain the behavior of the coupling function $\ln A(\rho)$ in terms of the matter density,

$$\rho \gg \rho_\alpha : \quad \ln A(\rho) \sim \alpha \left(\frac{\zeta\rho}{\rho_\alpha}\right)^{-\zeta/(1+\zeta)}, \qquad (101)$$

$$\rho \ll \rho_\alpha : \quad \ln A(\rho) \simeq \alpha \left(1 - 2\zeta^2 \frac{\rho}{\rho_\alpha}\right). \qquad (102)$$

As shown in the companion paper, the derived function $\ln A(\rho)$ is particularly important when applied to static configurations and can be used to probe the existence of a screening mechanism for this theory as we will show in sec.V A.

We show in Fig. 1 the characteristic functions that define the super-chameleon models and the associated ultra-local models, for the choice of chameleon exponents $\gamma = 2, \omega = 1, n = 2$ for the Kähler potential K and the superpotential W, and $\sigma = 1, 2, 3$ for the interaction potential $W_{\rm int}$. This gives $\zeta = 1/2, 1, 3/2$ for the ultra-local coupling function $\ln A(\tilde\chi)$. The left panel shows the normalized chameleon potential $V/\mathcal{M}^4$, which is also equal to the opposite of the ultra-local field $\tilde\chi$ from Eq.(76). It is identical for the three models that we consider in the numerical computations presented in this paper. The middle panel shows the chameleon coupling function $\ln A(\varphi)$ for the three choices for the exponent σ. The right panel shows the ultra-local coupling function $\ln A(\tilde\chi)$ for the corresponding three choices of the exponent ζ. In terms of the ultra-local model, or for the dynamics of cosmological perturbation in the chameleon model over scales $H \ll k/a \ll m_{\rm eff}$, this function $\ln A(\tilde\chi)$ fully defines the system.

In the right panel of Fig. 1 we show the coupling function $\ln A$ as a function of the normalized scalar field φ for different values of the parameter ζ. For all the models we have $|\bar A - 1| \lesssim 10^{-6} \ll 1$ which means that we recover the Λ-CDM cosmology at the background level to

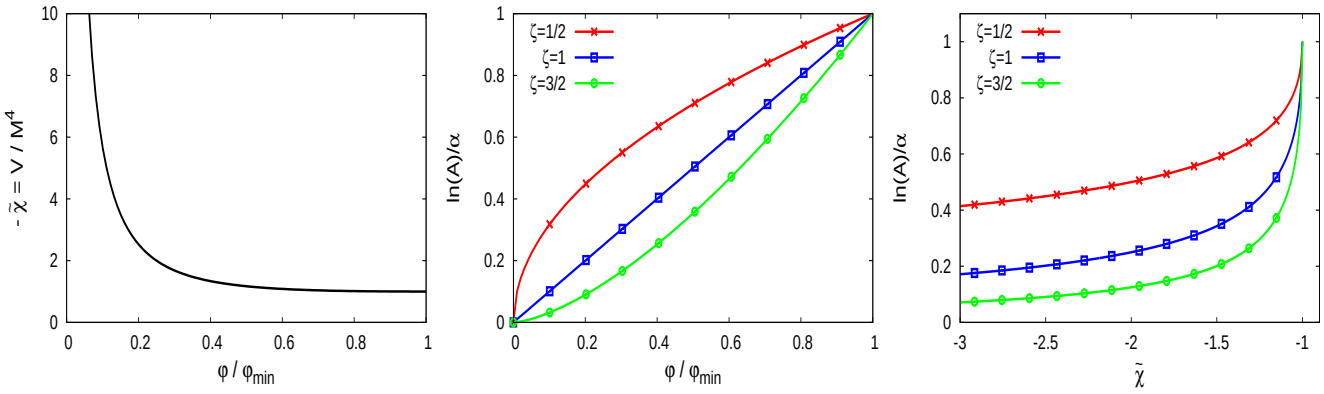

FIG. 1: *Left panel:* ultra-local scalar field or chameleon potential, $-\tilde{\chi} = V/\mathcal{M}^4$, as a function of the chameleon scalar field $\varphi/\varphi_{\rm min}$, as in Eq.(77) for $\gamma = 2, n = 2$. *Middle panel:* coupling function $\ln A(\varphi)$ as a function of the chameleon scalar field from Eq.(27), with $\gamma = 2$, $\sigma = 1, 2, 3$, which corresponds to $\zeta = 1/2, 1, 3/2$ with $n = 2$. *Right panel:* coupling function $\ln A(\tilde{\chi})$ as a function of the ultra-local scalar field $\tilde{\chi}$ from Eq.(95), for $\zeta = 1/2, 1, 3/2$.

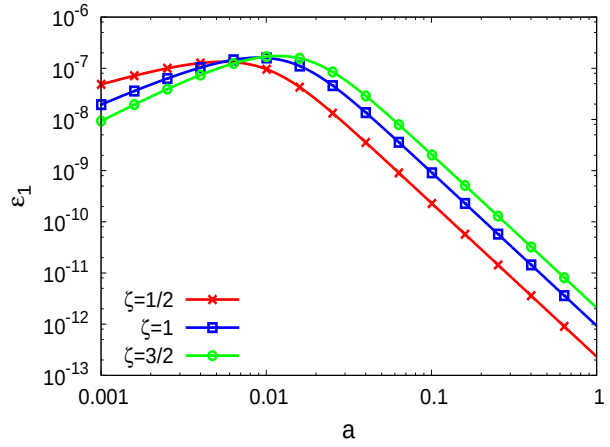

FIG. 2: Time evolution of the factor $\epsilon_1(a)$ as a function of the scale factor for $\zeta = 1/2, 1, 3/2$.

a 10^{-6} accuracy: in particular as we increase ζ the coupling function becomes steeper making the effect of the presence of the scalar field on the growth of structure more relevant, as we will demonstrate in section IV B.

B. Cosmological background and perturbations

For all the models we have $|\bar{A} - 1| \lesssim 10^{-6} \ll 1$, which means that we recover the Λ-CDM cosmology at the background level to a 10^{-6} accuracy. Therefore, to distinguish such models from the Λ-CDM scenario we must consider the dynamics of cosmological perturbations. As we can see from Eq.(70), the linear growth $D_+(k,t)$ of the dark matter density contrast is modified with respect to the Λ-CDM case only by the presence of the factor $\epsilon(k,t)$, which for the models presented in the previous sections is equal to

$$\epsilon_1 = 2\alpha\zeta \frac{\sqrt{-1-\tilde{\chi}}\left(1+\sqrt{-1-\tilde{\chi}}\right)^{-2\zeta}}{1+2(\zeta+1)\sqrt{-1-\tilde{\chi}}}, \qquad (103)$$

where we used the definition (68). From Eq.(98) and (99) we have the following simplified expressions for ϵ_1 as function of the density

$$\rho \gg \rho_\alpha : \quad \epsilon_1(\rho) \sim \frac{\alpha\zeta}{1+\zeta}\left(\frac{\zeta\rho}{\rho_\alpha}\right)^{-\zeta/(1+\zeta)}, \qquad (104)$$

$$\rho \ll \rho_\alpha : \quad \epsilon_1(\rho) \sim 2\alpha\zeta^2\frac{\rho}{\rho_\alpha}. \qquad (105)$$

This explicitly shows that ϵ_1 decreases both at high and low densities and peaks around ρ_α. This also gives the evolution of $\epsilon_1(t)$ as a function of the scale factor $a(t)$ using $\bar{\rho} = \bar{\rho}_0 a^{-3}$,

$$a \ll a_\alpha = \alpha^{1/3} : \quad \epsilon_1(a) \sim \alpha\left(\frac{a}{a_\alpha}\right)^{3\zeta/(1+\zeta)}, \qquad (106)$$

$$a \gg a_\alpha = \alpha^{1/3} : \quad \epsilon_1(a) \sim \alpha\left(\frac{a}{a_\alpha}\right)^{-3}, \qquad (107)$$

which peaks at the scale factor a_α that corresponds to $\bar{\rho} = \rho_\alpha$. In Fig. 2 we show the evolution of ϵ_1, for $\zeta = 1/2, 1, 3/2$, as a function of the scale factor. It is always positive for these models leading to an amplification of the Newtonian gravity. We can check that ϵ_1 has a maximum around $a_\alpha = \alpha^{1/3}$, which for this paper corresponds to a value of $a_\alpha = 0.01$. At low redshifts we recover the same decrease as $\epsilon_1 \propto a^{-3}$ of Eq.(107), whereas at high redshift the decrease is stronger for higher exponent ζ, in agreement with Eq.(106). At its peak at

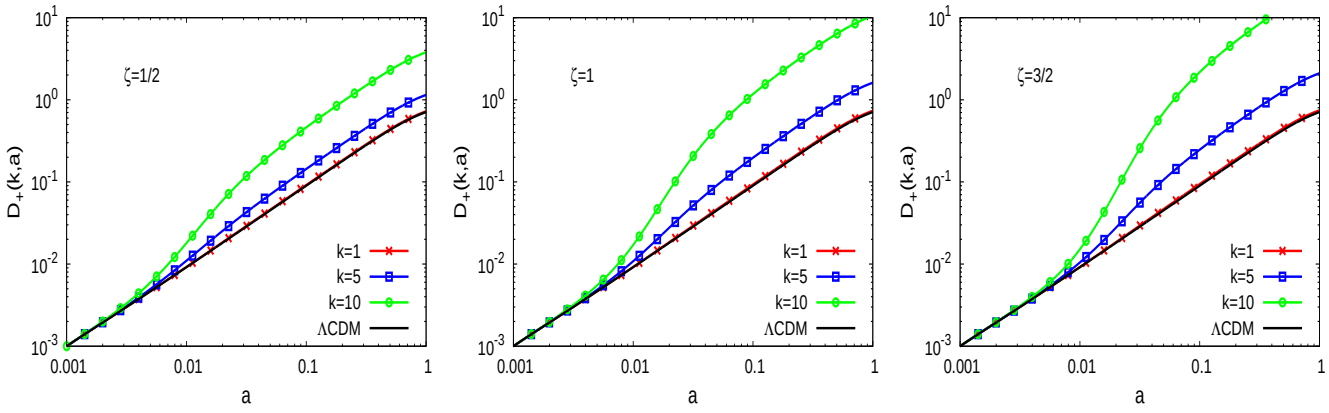

FIG. 3: Linear growing mode $D_+(k,a)$ for the models defined by Eq.(95), as a function of the scale factor for $k = 1, 5$ and $10\,h\mathrm{Mpc}^{-1}$, and for the Λ-CDM cosmology. We consider the cases $\zeta = 1/2, 1$ and $3/2$ (respectively left, center and right panel).

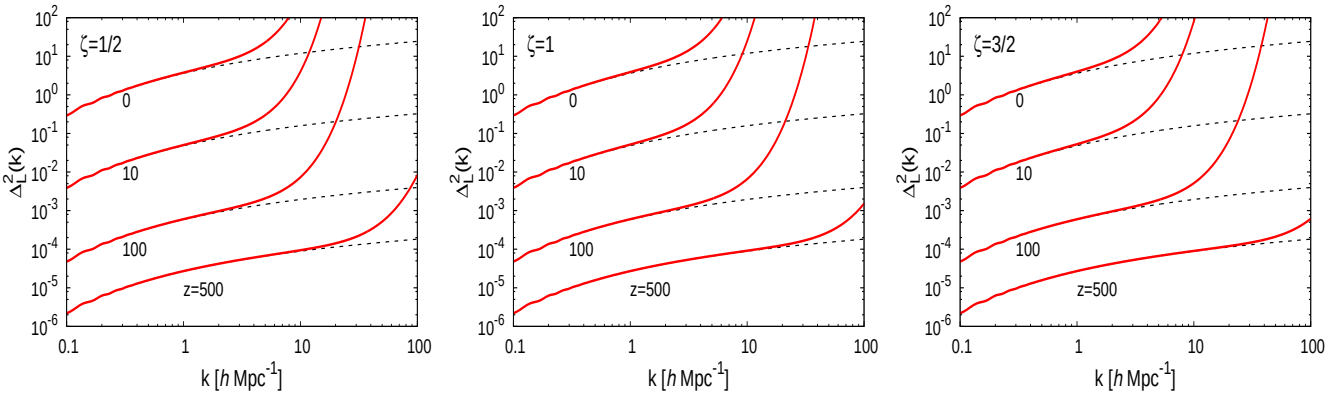

FIG. 4: Logarithmic linear power spectra $\Delta^2_L(k,z)$ at redshifts $z = 0, 10, 100$ and 500 (from top to bottom) at fixed $\zeta = 1/2, 1$ and $3/2$ (respectively left, center and right panel).

a_α, we have $\epsilon_1 \sim \alpha = 10^{-6}$, whereas today we have $\epsilon_1 \sim \alpha^2 = 10^{-12}$.

As shown in the companion paper, the growth of structure is vastly enhanced by the presence of the scalar field when $\epsilon(k,a) \gg 1$ in Eq.(70). Because $\epsilon(k,a)$ grows as k^2 at high k, there exists a time dependent scale $k_\alpha(a)$ such that for any scale smaller than the latter $D_+(k,a)$ deviates significantly from the Λ-CDM one. This threshold $k_\alpha(a)$ can be computed from the condition $\epsilon[k_\alpha(a), a] = 1$ in Eq.(71), to obtain

$$k_\alpha(a) = \frac{aH}{c\sqrt{\epsilon_1}} \sim \frac{H_0}{c\sqrt{\epsilon_1 a}}, \tag{108}$$

where we used $H^2 \propto a^{-3}$ in the matter era. Because ϵ_1 decreases at both high and low redshifts, with a peak at a_α, the threshold $k_\alpha(a)$ is minimum at the scale factor a_α,

$$k^{\rm min}_\alpha = k_\alpha(a_\alpha) \sim \frac{H_0}{c\,\alpha^{2/3}} \sim 3h\mathrm{Mpc}^{-1}, \tag{109}$$

Therefore, low wave numbers $k < k^{\rm min}_\alpha$ are never sensitive to the fifth force whereas high wave numbers $k > k^{\rm min}_\alpha$ are sensitive to the fifth force around a_α. The range of scale factors $[a_-(k), a_+(k)]$ where a wave number k feels the fifth force broadens at higher k. From Eq.(108) we obtain

$$k > k_{\rm min}: \quad a_-(k) \sim a_\alpha \left(\frac{k}{k_{\rm min}}\right)^{-(2\zeta+2)/(4\zeta+1)}, \tag{110}$$

$$a_+(k) \sim a_\alpha \frac{k}{k_{\rm min}}. \tag{111}$$

In Fig. 3 we show the evolution of the linear growing mode $D_+(k,a)$ obtained numerically solving Eq.(70) at three different scales, for the models considered in this paper. In agreement with the discussion of Eq.(109) above, low wave numbers $k < k^{\rm min}_\alpha$ are never sensitive to the fifth force and follow the Λ-CDM growth. Higher wave numbers depart from the Λ-CDM behavior around

$a_\alpha \sim 0.01$ and show a faster growth over a limited time range $[a_-, a_+]$, resuming the Λ-CDM growth at later times. This transient speed-up increases with k. This effect becomes stronger at higher ζ because of the higher amplitude of ϵ_1 found in Fig. 2.

The presence of the scalar field leads to a very steep increase of $D_+(k,a)$ at $k \gg 1\,h$ Mpc^{-1} and so these scales enter the nonlinear regime much earlier than in the Λ-CDM cosmology, at $z \sim z_\alpha$. This can be seen in Fig. 4 where we plot the logarithmic linear power spectrum $\Delta_L^2(k,z) = 4\pi k^3 P_L(k,z)$.

C. Spherical collapse

On large scales where the baryonic pressure is negligible, the particle trajectories $\mathbf{r}(t)$ follow the equation of motion

$$\frac{d^2\mathbf{r}}{dt^2} - \frac{1}{a}\frac{d^2a}{dt^2}\mathbf{r} = -\nabla_{\mathbf{r}}\left(\Psi_{\rm N} + \Psi_A\right), \qquad (112)$$

where $\mathbf{r} = a\mathbf{x}$ is the physical coordinate, $\Psi_{\rm N}$ the Newtonian potential and $\Psi_A = c^2 \ln A$ the fifth-force potential. To study the spherical collapse before shell crossing, it is convenient to label each shell by its Lagrangian radius q or enclosed mass M, and to introduce its normalized radius $y(t)$ by

$$y(t) = \frac{r(t)}{a(t)q} \quad \text{with} \quad q = \left(\frac{3M}{4\pi\bar\rho_0}\right)^{1/3}, \quad y(t=0) = 1. \qquad (113)$$

In particular, the matter density contrast within radius $r(t)$ reads as

$$1 + \delta_<(r) = y(t)^{-3}. \qquad (114)$$

The equation of motion becomes

$$\frac{d^2y}{d(\ln a)^2} + \left(2 + \frac{1}{H^2}\frac{dH}{dt}\right)\frac{dy}{d\ln a} + \frac{\Omega_{\rm m}}{2}y(y^{-3}-1) = -y\left(\frac{c}{Hr}\right)^2 \frac{d\ln A}{d\ln\rho}\frac{r}{1+\delta}\frac{\partial\delta}{\partial r}. \qquad (115)$$

The fifth force introduces a coupling as it depends on the density profile, through the local density $\rho(r) = \bar\rho(1+\delta(r))$.

In the following, we use the density profile defined by

$$\delta(x') = \frac{\delta_<(x)}{\sigma_x^2}\int_V \frac{d\mathbf{x}''}{V}\,\xi_L(\mathbf{x}', \mathbf{x}'') = \frac{\delta_<(x)}{\sigma_x^2}\int_0^{+\infty}\frac{dk}{k}\,\Delta_L^2(k)\tilde W(kx)\frac{\sin(kx')}{kx'}. \qquad (116)$$

Here $x(t) = a(t)r(t)$ is the comoving radius of the spherical shell of mass M that we are interested in while x' is any radius along the profile; ξ_L and Δ_L^2 are the linear correlation function and logarithmic power spectrum of the matter density contrast, $\sigma_x^2 = \langle\delta_{L<}(x)^2\rangle$ its variance within radius x, which defines a sphere of volume V; and $\tilde W(kx) = 3[\sin(kx) - kx\cos(kx)]/(kx)^3$ the Fourier transform of the 3D top hat of radius x. The profile (116) is the typical profile around a density fluctuation at scale x in the initial Gaussian field and provides a convenient ansatz (here we use the initial linear power spectrum or its Λ-CDM amplified value at the redshift of interest).

We show in Fig. 5 the time evolution of the nonlinear density contrast $\delta_<(r)$ within a shell of mass M, given by the spherical dynamics (115), for different values of the mass M, fixing the initial linear density contrast so that $\delta_L^{\Lambda-{\rm CDM}} = 1.6$ today (the initial condition is set at high redshift before the onset of the fifth force and it is common to all models and the Λ-CDM cosmology; as usual it is convenient to describe this initial condition by its value today using the Λ-CDM linear growth factor). In agreement with what we found by studying the evolution of linear perturbations, we can see that at large masses, $M \gtrsim 10^{12}h^{-1}M_\odot$, the evolution of $\delta_<(r)$ closely follows the Λ-CDM one, whereas the collapse of small masses is strongly accelerated around a_α. This faster growth occurs earlier for smaller mass, as $a_-(k)$ decreases on smaller scales.

We show in Fig. 6 the spherical dynamics for a fixed value of the mass $M = 10^8h^{-1}M_\odot$ and several initial density contrasts. The acceleration of the growth of structure due to the presence of the scalar field makes halos collapse before $a = 1$, even starting from $\delta_L^{\Lambda-{\rm CDM}} \simeq 0.1$. In agreement with previous figures, the acceleration of the collapse occurs around a_α. For sufficiently high initial conditions this leads to a collapse at high redshift around z_α. For lower initial conditions the dynamics is still in the linear regime after the fifth force has vanished, at low redshift, but with a higher amplitude than in the Λ-CDM cosmology and a higher final collapse redshift. Again, we can see that the effect of the fifth force increases with ζ.

We show in the upper panel of Fig. 7 the linear density contrast threshold, measured by $\delta_L^{\Lambda-{\rm CDM}}$ (i.e., the extrapolation up to $z = 0$ of the linear initial density contrast by the Λ-CDM growth rate), required to reach a nonlinear density contrast $\delta_< = 200$ today. In agreement with Figs. 5 and 6, at large mass we recover the Λ-CDM linear density threshold, $\delta_L^{\Lambda-{\rm CDM}} \simeq 1.6$, whereas at small mass we obtain a much smaller linear density threshold, $\delta_L^{\Lambda-{\rm CDM}} \ll 1$, because of the acceleration of the collapse by the fifth force. Again, at small masses the threshold δ_L becomes smaller for larger exponent ζ as the effect of the fifth force increases.

D. Halo mass function

As for the Λ-CDM cosmology, we write the comoving halo mass function as

$$n(M)\frac{dM}{M} = \frac{\bar\rho_0}{M}f(\nu)\frac{d\nu}{\nu}, \qquad (117)$$

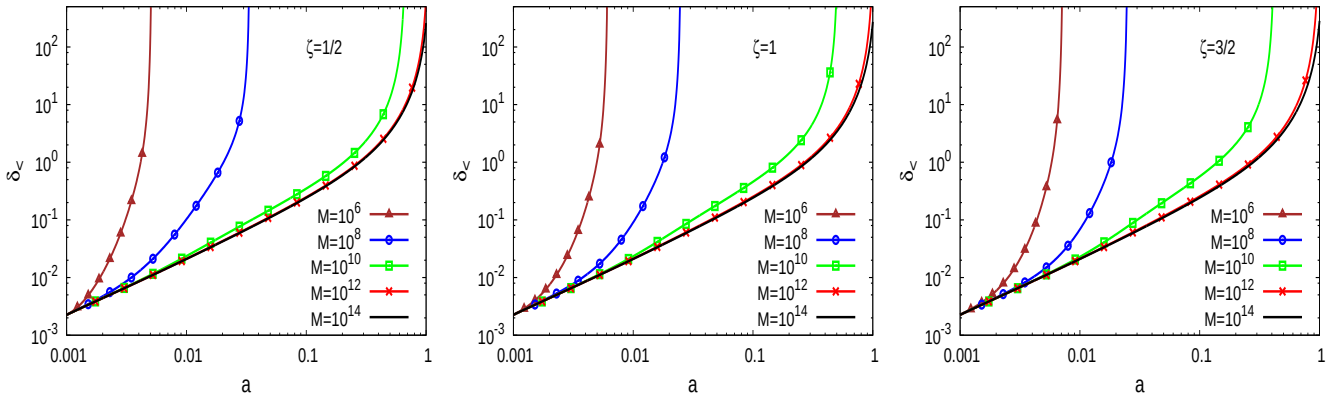

FIG. 5: Time evolution of the nonlinear density contrast $\delta(< r)$ given by the spherical dynamics, as a function of the scale factor, for several masses (in units of $h^{-1}M_\odot$) at fixed $\zeta = 1/2, 1, 3/2$ (respectively left, center and right panel). The initial condition corresponds to the same linear density contrast $\delta_L^{\Lambda-\rm CDM} = 1.6$ today, using the Λ-CDM growth factor.

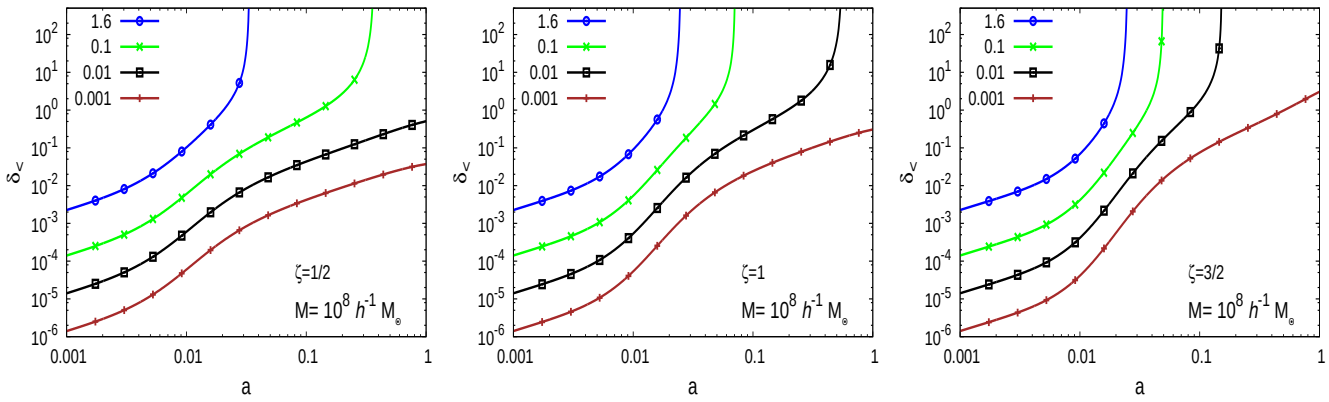

FIG. 6: Time evolution of the nonlinear density contrast $\delta(< r)$ given by the spherical dynamics, as a function of the scale factor, for several values of the initial density contrast and for a mass of $M = 10^8 h^{-1} M_\odot$ at fixed $\zeta = 1/2, 1, 3/2$(respectively left, center and right panel). We show our results for different initial conditions, which correspond to $\delta_L^{\Lambda-\rm CDM} = 1.6, 0.1, 0.01$ and 0.001 from top to bottom.

where the scaling variable $\nu(M)$ is defined as

$$\nu(M) = \frac{\delta_L^{\Lambda-\rm CDM}(M)}{\sigma^{\Lambda-\rm CDM}(M)}, \qquad (118)$$

and $\delta_L^{\Lambda-\rm CDM}(M)$ is again the initial linear density contrast (extrapolated up to $z = 0$ by the Λ-CDM linear growth factor) that is required to build a collapsed halo (which we define here by a nonlinear density contrast of 200 with respect to the mean density of the Universe) and $\sigma^{\Lambda-\rm CDM}$ its variance. The variable ν measures whether such an initial condition corresponds to a rare and very high overdensity in the initial Gaussian field ($\nu \gg 1$) or to a typical fluctuation ($\nu \lesssim 1$). In the Press-Schechter approach, we have $f(\nu) = \sqrt{2/\pi}\nu e^{-\nu^2/2}$. Here we use the same function as in [28]. Then, the impact of the modified gravity only arises through the linear threshold $\delta_L^{\Lambda\rm CDM}(M)$, as we assume the same initial matter density power spectrum as for the Λ-CDM reference at high redshift.

The threshold $\delta_L^{\Lambda-\rm CDM}(M)$ was shown in the upper panel of Fig. 7. We show the mass function in the lower panel of Fig. 7. Once again, we can notice that at large mass all the mass functions are close to the Λ-CDM prediction whereas at smaller masses, $M \sim 10^8 - 10^{10} h^{-1} M_\odot$, they are higher. This is because the fifth force has no effect on very large scales and accelerates the formation of structures on small scales. At lower mass, $M \lesssim 10^7 h^{-1} M_\odot$, the mass function becomes smaller than in the Λ-CDM cosmology, because both mass functions are normalized to unity (the sum over all halos cannot give more matter than the mean matter density).

At large masses, $M > 10^{12} h^{-1} M_\odot$, where the formation of large-scale structures remains close to the Λ-CDM

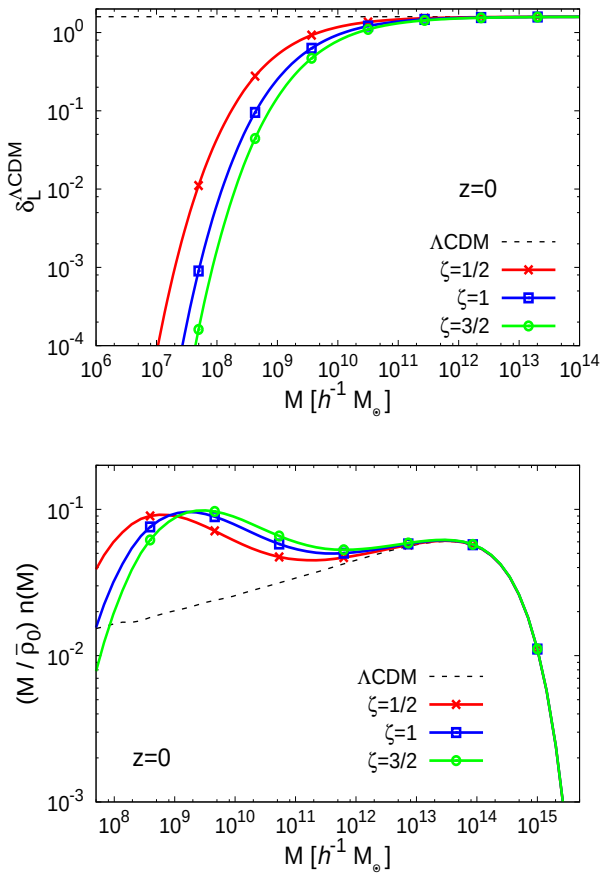

FIG. 7: *Upper panel:* Initial linear density contrast, as measured by $\delta_L^{\Lambda-\mathrm{CDM}}$, that gives rise to a nonlinear density contrast $\delta_< = 200$ at $z = 0$, as a function of the halo mass M for fixed $\zeta = 1/2, 1$ and $3/2$. *Lower panel:* Halo mass function at $z = 0$ for fixed $\zeta = 1/2, 1$ and $3/2$, and for the ΛCDM cosmology.

case, with only a modest acceleration, and the mass function is dominated by the Gaussian tail $\sim e^{-\nu^2/2}$, we can expect that the results obtained are robust, since in this regime the shape of the halo mass function is dominated by the exponential tail $e^{-\nu^2/2}$. At low masses, $M < 10^{12}h^{-1}M_\odot$, where the history of gravitational clustering is significantly different from the Λ-CDM scenario, as a large range of masses have collapsed together before a redshift of 100, and the halo mass function is no longer dominated by its universal Gaussian tail, these results are unlikely to be accurate. Nevertheless, we can still expect the halo mass function to be significantly higher than in the Λ-CDM case for masses $M \sim 10^8 - 10^{11}h^{-1}M_\odot$, although it is difficult to predict the maximum deviation and the transition to a negative deviation at very low masses.

V. ASTROPHYSICAL EFFECTS

A. Screening within spherical halos

1. Radial profiles

We first consider here how the ratio of the fifth force to Newtonian gravity behaves within spherical halos with a mean density profile such as the Navarro-Frenk-White (NFW) [29] density profile. In particular, we wish to find the conditions for the fifth force not to diverge at the center of the halos and to remain modest at all radii, to be consistent with observations of X-ray clusters. Within spherical halos, the Newtonian force reads as

$$F_{\rm N} = -\frac{\mathcal{G}_{\rm N}M(<r)}{r^2} = -\frac{\Omega_{\rm m}}{2}\Delta(<r)rH^2, \qquad (119)$$

where $\Delta(<r)$ is the mean overdensity within radius r. The fifth force reads

$$F_A = -c^2\frac{d\ln A}{dr} = -\frac{c^2}{r}\frac{d\ln A}{d\ln\rho}\frac{d\ln\rho}{d\ln r}. \qquad (120)$$

We can also use $F_{\rm N}$ and F_A to define characteristic velocity scales,

$$F_{\rm N} = -\frac{v_{\rm N}^2(r)}{r}, \quad F_A = -\frac{c_s^2(r)}{r}, \qquad (121)$$

with

$$v_{\rm N}^2 = \frac{\mathcal{G}_{\rm N}M(<r)}{r}, \quad c_s^2 = c^2\frac{d\ln A}{d\ln r}, \qquad (122)$$

where $v_{\rm N}$ is the Newtonian circular velocity. Therefore, the ratio of the fifth force to the Newtonian force is

$$\eta \equiv \frac{F_A}{F_{\rm N}} = \frac{c_s^2}{v_{\rm N}^2} = \frac{2}{\Omega_{\rm m}\Delta(<r)}\left(\frac{c}{rH}\right)^2\frac{d\ln A}{d\ln\rho}\frac{d\ln\rho}{d\ln r}. \qquad (123)$$

From Eq.(102), we have at moderate densities, $\rho \sim \bar\rho(z)$,

$$\rho \ll \rho_\alpha : \quad |\eta| \sim \frac{\alpha^2\zeta^2}{a^3}\left(\frac{c}{rH}\right)^2. \qquad (124)$$

Thus, in the late Universe the ratio η is suppressed by a factor α^2 so that η only reaches unity at $r \sim 3h^{-1}$kpc, i.e. at galaxy scales (see also Sec. V A 3 below). At higher densities, we obtain from Eq.(101)

$$\rho \gg \rho_\alpha : |\eta| \sim \frac{\alpha^2\zeta}{a^3}\left(\frac{a^3}{\alpha\zeta\Delta}\right)^{(1+2\zeta)/(1+1\zeta)}\left(\frac{c}{rH}\right)^2. \qquad (125)$$

We plot the ratio η for several halo masses, with an NFW density profile in Fig. 8. In agreement with the results obtained in previous sections, we can see that the fifth force is more important for smaller halos, which also correspond to smaller scales. For a power-law density profile, of exponent $\gamma_p > 0$ and critical radius r_α,

$$\rho(r) = \rho_\alpha\left(\frac{r}{r_\alpha}\right)^{-\gamma_p}, \qquad (126)$$

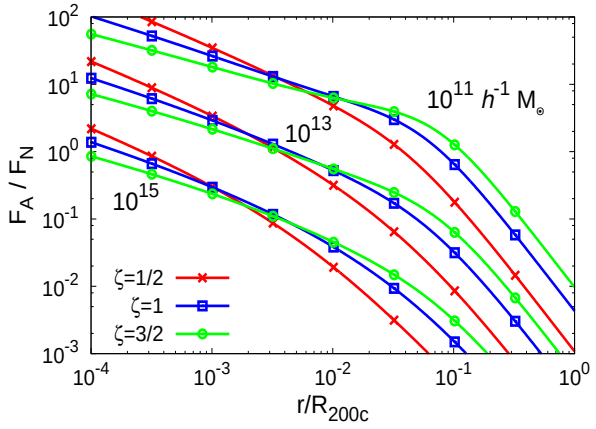

FIG. 8: Ratio $\eta = F_A/F_N$ as a function of the radius r, within spherical halos with an NFW profile. We display the cases of halo masses $M = 10^{11}, 10^{13}$ and $10^{15} h^{-1} M_\odot$ from top to bottom, for the ultra-local model exponent $\zeta = 1/2, 1$ and $3/2$.

we have

$$r < r_\alpha, \quad \eta \sim r^{\gamma_p(1+2\zeta)/(1+\zeta)-2}. \tag{127}$$

If we consider halos with a mean NFW density profile, which has $\gamma_p = 1$, we find that $\eta \sim r^{-1/(1+\zeta)}$ and the relative importance of the fifth force does not vanish at the center for the models, whatever the value of the exponent ζ, in agreement with Fig. 8. This suggests that these models would lead to significant modifications in the cluster dynamics with respect to the Λ-CDM model and so would be ruled out by the observations, which show a good agreement with the Λ-CDM cosmology. However, as we can see from Fig. 8, for typical cluster masses η only becomes of the order of unity far within the virial radius, $r \lesssim 0.01 R_{200c}$ for $M \gtrsim 10^{13} h^{-1} M_\odot$. Because at these scales clusters have significant substructures the approximation of a smooth profile is not any more correct. Then, deeper analyses are needed to unravel the dynamics of clusters of galaxies considering the ultra-local behaviour of the theory. We leave these analysis for future studies when we may need to use numerical simulations and to estimate the observational accuracy of the measured halo profiles. On the other hand, we will perform a thermodynamic analysis of the system in VI where we find that for large enough clusters, the mean density approximation is valid.

2. *Clusters of galaxies*

We now estimate the fifth force to Newtonian gravity ratio η on a global scale, for clusters and for galaxies. In contrast with the companion paper, we do not need to study the Solar System, the Earth or the laboratory, because within the supersymmetric setting considered in this paper baryons do not couple to the fifth force. Therefore, astrophysical systems which are dominated by baryons do not feel the effect of the fifth force and we automatically recover the General Relativity or Newtonian dynamics in these systems.

We have seen in Eq.(123) that $\eta = c_s^2/v_N^2$, whence $\eta \sim (c/v_N)^2 |d\ln A/d\ln\rho|$ if we take $d\ln\rho/d\ln r \sim 1$. From Eq.(102), we also have at moderate densities below $\rho_\alpha \sim 10^6 \bar\rho_0$, $d\ln A/d\ln\rho \sim -\alpha^2\Delta$ at redshift $z = 0$. This gives

$$z = 0: \quad \eta \sim \left(\frac{\alpha c}{v_N}\right)^2 \Delta. \tag{128}$$

For clusters of galaxies, with $\Delta \sim 10^3$ and $v_N \sim 500$ km/s, this yields

$$\text{clusters:} \quad \eta \sim (10^4\,\alpha)^2 \ll 1. \tag{129}$$

Therefore, the fifth force is negligible on cluster scales. However, as seen in Fig. 8, this is no longer the case far inside the cluster, where the characteristic scales are smaller and the density greater, which gives rise to a greater fifth force.

3. *Galaxies*

We now consider a typical galaxy, such as the Milky Way, with $\Delta \sim 10^6$, which is at the upper limit of the regime $\rho \lesssim \rho_\alpha$, and $v_N \sim 200$ km/s. This gives

$$\text{galaxies:} \quad \eta \sim (10^6\,\alpha)^2 \sim 1. \tag{130}$$

Thus, the fifth force is of the same order as the Newtonian gravity on galaxy scales. This suggests that interesting phenomena could occur in this regime and that galaxies could provide a useful probe of such models, as we can see from Fig. 8 for low-mass halos $M \lesssim 10^{11} h^{-1} M_\odot$.

B. Fifth-force dominated regime

It is useful to reformulate the analysis presented above for clusters and galaxies and to determine the domain of length, density and mass scales where the fifth force is dominant. Taking $d\ln\rho/d\ln r \sim 1$, we write for structures of typical radius R, density ρ and mass $M = 4\pi\rho R^3/3$,

$$|\eta| \sim \frac{2}{\Omega_{m0}} \frac{\bar\rho_0}{\rho} \left(\frac{c}{R H_0}\right)^2 \left|\frac{d\ln A}{d\ln\rho}\right|. \tag{131}$$

Then, the fifth force is greater than Newtonian gravity if we have

$$|\eta| \geq 1: \quad R^2 \leq R_\eta^2 \equiv \left(\frac{c}{H_0}\right)^2 \frac{2}{\Omega_{m0}} \frac{\bar\rho_0}{\rho} \left|\frac{d\ln A}{d\ln\rho}\right|. \tag{132}$$

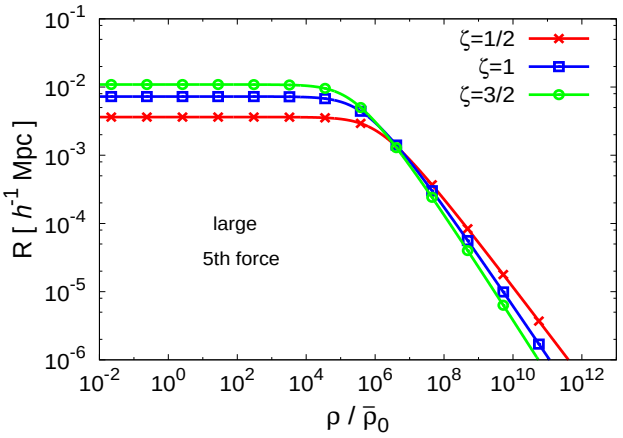

FIG. 9: Domain in the density-radius plane where the fifth force is greater than Newtonian gravity (bottom left area below the curves), for the ultra-local exponents $\zeta = 1/2, 1$ and $3/2$.

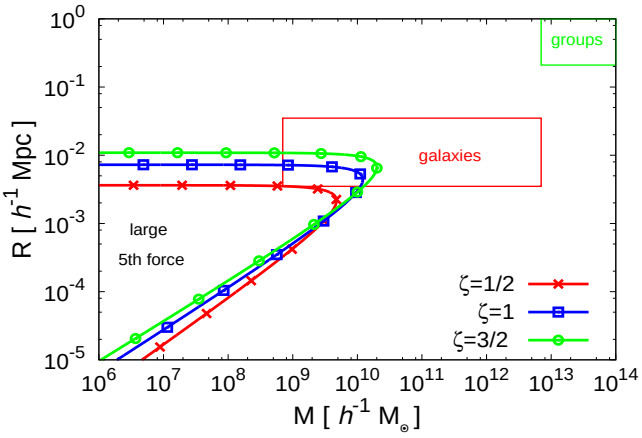

FIG. 10: Domain in the mass-radius plane where the fifth force is greater than Newtonian. The horizontal axis is the typical mass M of the structure and the vertical axis its typical radius R. The rectangles show the typical scales of galaxies and groups of galaxies.

At low densities, using Eq.(102) we obtain

$$\rho \ll \rho_\alpha : \quad R_\eta(\rho) \sim R_\alpha \ \text{ with } \ R_\alpha \equiv \frac{\alpha\,\zeta\,c}{H_0}. \tag{133}$$

Thus, at low densities we obtain a constant radius threshold, of order $R_\alpha \sim 3h^{-1}\,\mathrm{kpc}$ for $\alpha = 10^{-6}$, which grows with ζ as we can check in Fig. 9. At high densities, we have the behaviour

$$\rho \gg \rho_\alpha : \quad R_\eta \sim R_\alpha \left(\frac{\rho}{\rho_\alpha}\right)^{-(2\zeta+1)/(2\zeta+2)}. \tag{134}$$

Thus, at high densities the upper boundary of the fifth-force domain decreases and the fifth force becomes negligible in the center of halos with sufficiently steep profiles, as seen in Eq.(127).

To facilitate the comparison with astrophysical structures, it is convenient to display the fifth-force domain (132) in the mass-radius plane (M, R). This is shown in Fig. 10, as the curve $R_\eta(\rho)$ provides a parametric definition of the boundary $R_\eta(M)$, defining the mass of the structure as $M = 4\pi\rho R^3/3$. We obtain a triangular domain, with a constant-radius upper branch and a lower branch that goes towards small radius and mass with a slope that depends on ζ. The upper branch corresponds to the regime (133), with

$$R_\eta \sim R_\alpha \quad \text{for} \quad M < M_\alpha, \tag{135}$$

and

$$M_\alpha \equiv \alpha^2\zeta^3\bar{\rho}_0\left(\frac{c}{H_0}\right)^3. \tag{136}$$

For $\alpha = 10^{-6}$ this yields $M_\alpha \sim 10^{10}M_\odot$. The lower branch corresponds to the regime (134), which yields for $M < M_\alpha$

$$R \sim R_\alpha \left(\frac{M}{M_\alpha}\right)^{(2\zeta+1)/(4\zeta+1)}. \tag{137}$$

We also show in Fig. 10 the regions in this (M, R)-plane occupied by groups and clusters of galaxies and by galaxies. We only show astrophysical objects whose dynamics is due to the presence of dark matter since for this model the coupling of the scalar field with baryons is negligible, as shown in section II G. In agreement with section V A, we find that the fifth force is negligible for clusters and groups (at their global scale), while it is of the same order as Newtonian gravity for galaxies. Therefore galaxies may provide strong constraints on the models considered in this paper.

VI. HISTORY AND PROPERTIES OF THE FORMATION OF COSMOLOGICAL STRUCTURES

To study the evolution of cosmological perturbations in the previous sections, either through linear theory or the spherical collapse, we assumed that the density field remains smooth and that the fifth force on cosmological scale x is set by the density gradient on the same scale. However, the ultra-local fifth force is directly sensitive to the local density gradient, $\nabla \ln A = (d\ln A/d\ln\rho)\nabla\rho$, in contrast with the Newtonian force which involves an average over scale x, $F_\mathrm{N} \propto \int d\mathbf{x}'\rho(\mathbf{x}')/|\mathbf{x}-\mathbf{x}'|^2$. Moreover, smaller scales are increasingly unstable because of the k^2 factor in the factor $\epsilon(k,\tau)$ in Eq.(71) that amplifies the gravitational attraction in the linear evolution equation (70). This could invalidate the analysis presented

above as small scales could develop strong instabilities. This would lead to a fragmentation of the system down to very small scales so that the local density gradient, hence the fifth force, is nowhere related to cosmological scale gradients. This would in turn lead to an effective screening mechanism as isolated overdensities no longer interact. Note that this mechanism, due to the ultra-local character of the theory, is the key to the screening of the fifth force in local environments, such as in the Solar System, which is required in the theories studied in the companion paper where both the baryons and the dark matter feel the fifth force. In the supersymmetric setting considered in this paper, we do not need to invoke this mechanism to ensure that the theory is consistent with Solar System tests as the baryons do not feel the fifth force. However, it could still play a role in case it leads to a fragmentation of the dark matter density field at high redshift, when the fifth force is dominant, and makes a "mean field" approach inadequate.

As described in details in the companion paper [14], we can investigate this issue by using a thermodynamic approach, which allows us to go beyond perturbation theory and spherical dynamics. Thus, we assume that at high redshift, when the fifth force is dominant, regions that collapse and turn non-linear because of the fifth-force interaction relax towards the thermodynamic equilibrium. Then, if this equilibrium is strongly inhomogeneous the mean field approach used in the previous sections breaks down, whereas if this equilibrium is homogeneous we can conclude that the system does not develop strong small-scale inhomogeneities and the previous analysis is correct.

A. Cosmological non-linear transition

We first study in this section the evolution with redshift of the comoving cosmological scales $x_{\rm coll}(z)$ that enter the non-linear regime, which we define by

$$\Delta_L^2(\pi/x_{\rm coll}, z) = 1.5 \tag{138}$$

where Δ_L^2 is the logarithmic linear power spectrum. (The factor 1.5 is chosen so that we obtain $x_{\rm coll} \simeq 8h^{-1}$Mpc at $z = 0$ in the Λ-CDM scenario.) As seen in the upper panel in Fig. 11, $x_{\rm coll}(z)$ is much greater than in the Λ-CDM cosmology at high redshift because the fifth force amplifies the growth of structure. After a_α the fifth force fastly decreases, as seen in Fig. 2. This leads to the plateau for $x_{\rm coll}(z)$ over $a_\alpha \leq a \leq a_{\Lambda-{\rm CDM}}$, with $a_\alpha = \alpha^{1/3} \sim 0.01$ associated with the peak of the fifth force and $a_{\Lambda-{\rm CDM}} \simeq 0.2$ associated with the convergence to the Λ-CDM prediction for $x_{\rm coll}(z)$. The reason why $a_\alpha \ll a_{\Lambda-{\rm CDM}}$ is that after a_α the fast decrease of the fifth force implies that structure formation due to the fifth force stalls, and we need to wait until $a_{\Lambda-{\rm CDM}}$ for Newtonian gravity to take over at the scale $x_{\rm coll}(z_\alpha)$, because at a_α Newtonian gravity was much weaker than the fifth force at the comoving scale $x_{\rm coll}(z_\alpha)$. Thus, from the point of view of cosmological structure formation, we have three eras. For $a < a_\alpha$, the non-linear transition $x_{\rm coll}(z)$ of the cosmological density field is due to the fifth force and occurs at scales much greater than in the Λ-CDM scenario. For $a_\alpha < a < a_{\Lambda-{\rm CDM}}$, structure formation stalls as the fifth force decreases and Newtonian gravity is still weak on these scales. For $a_{\Lambda-{\rm CDM}} < a$, we recover the growth predicted by the Λ-CDM cosmology, due to Newtonian gravity.

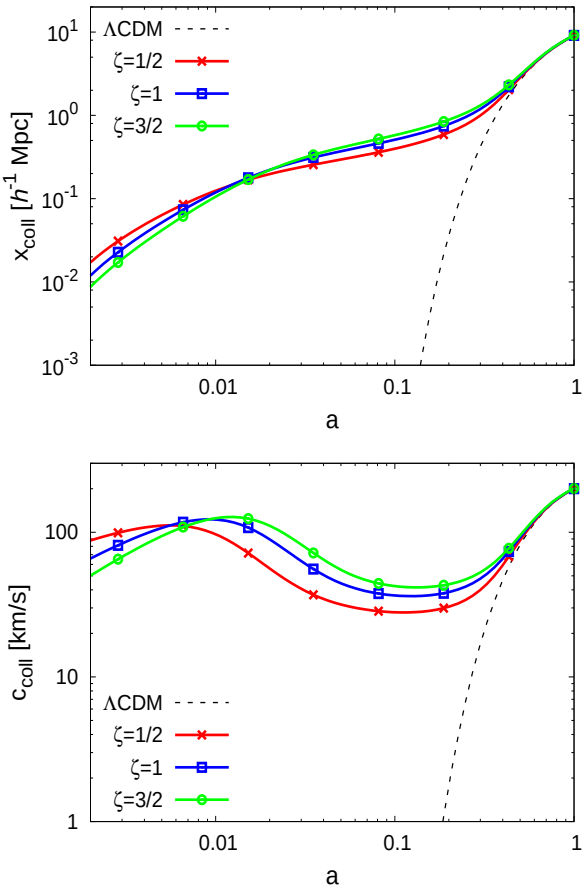

FIG. 11: *Upper panel:* collapse radius $x_{\rm coll}(z)$ (in comoving coordinates) as a function of the scale factor, for the ultra-local models and the Λ-CDM cosmology. *Lower panel:* collapse velocity scale $c_{\rm coll}(z)$.

For the thermodynamic analysis presented in the next section we also need the initial kinetic energy or typical velocity of the collapsing domains. Thus, we define the effective velocity $c_{\rm coll}(z)$ by

$$c_{\rm coll}^2(z) = c_s^2 + c_{\rm N}^2, \tag{139}$$

with

$$c_s^2 = \epsilon_1\, c^2, \quad c_{\rm N}^2 = (1+\epsilon_1)\frac{3\Omega_{\rm m}}{2\pi^2}(Hax_{\rm coll})^2. \tag{140}$$

The term c_s^2 comes from the pressure-like term $\epsilon_1 c^2\nabla^2\delta$ in Eq.(69) while the term $c_{\rm N}^2$ comes from the right-hand side

in Eq.(69), associated with Newtonian gravity (amplified by the negligible factor ϵ_1). In the case of the Λ-CDM cosmology we only have $c_{\rm coll}^{\Lambda-{\rm CDM}} = c_{\rm N}^{\Lambda-{\rm CDM}}$ as there is no fifth-force pressure-like term. As seen in the lower panel in Fig. 11, at high redshift, $a < a_{\Lambda-{\rm CDM}}$, we have $c_{\rm coll} \gg c_{\rm coll}^{\Lambda-{\rm CDM}}$, whereas at low redshift, $a_{\Lambda-{\rm CDM}} < a$, we have $c_{\rm coll} \simeq c_{\rm coll}^{\Lambda-{\rm CDM}}$ as we recover the Λ-CDM behavior. Between a_α and $a_{\Lambda-{\rm CDM}}$ the velocity scale first decreases until $a_{c_s/c_{\rm N}} \simeq 0.1$ with the decline of the fifth force, as $c_{\rm coll} \simeq c_s$, and next grows again with Newtonian gravity as $c_{\rm coll} \simeq c_{\rm N}$.

This history singles out a characteristic mass and velocity scale, associated with the plateau found in Fig. 11 over $0.02 \lesssim a \lesssim 0.2$. This yields

$$x_* \sim 0.355\, h^{-1}{\rm Mpc}, \quad M_* \sim 2\times 10^{10}\, h^{-1} M_\odot, \\ c_* \sim 50\ {\rm km/s}. \tag{141}$$

As in Fig. 10, we recover galaxy scales, more precisely here the scales associated with small galaxies. It is tempting to wonder whether this could help alleviate some of the problems encountered on galaxy scales by the standard Λ-CDM scenario. However, this would require detailed numerical studies that are beyond the scope of this paper.

B. Thermodynamic equilibrium on cosmological scales

We can now study the non-linear dynamics of the cosmological scales $x_{\rm coll}(z)$ that enter the non-linear regime found in Fig. 11. More precisely, we use a thermodynamic approach to investigate whether these regions develop a fragmentation process and show strong small-scale inhomogeneities [30, 31]. Because we are interested in the evolution at high redshift, $z \geq z_\alpha$, when the fifth force is dominant, we neglect the Newtonian gravity and we consider the thermodynamic equilibrium of systems defined by the energy E and entropy S given by

$$E = \int d^3x d^3v\ f(\mathbf{x},\mathbf{v}) \left(\frac{v^2}{2} + c^2 \ln A[\rho(\mathbf{x})]\right), \tag{142}$$

$$S = -\int d^3x d^3v\ f(\mathbf{x},\mathbf{v})\ \ln\frac{f(\mathbf{x},\mathbf{v})}{f_0}. \tag{143}$$

Here $f(\mathbf{x},\mathbf{v})$ is the phase-space distribution function, f_0 is an irrelevant normalization constant, and we used the fact that the fifth-force potential $\ln A$ is a function of the local density. Then, assuming that the scales that turn non-linear because of the fifth force at high redshift reach a statistical equilibrium through the rapidly changing effects of the fluctuating potential, in a fashion somewhat similar to the violent relaxation that takes place for gravitational systems [32], we investigate the properties of this thermodynamic equilibrium.

Contrary to the usual gravitational case, the potential $\ln A$ is both bounded and short-ranged , so that we cannot build infinitely large negative (or positive) potential energies and a stable thermodynamic equilibrium always exists, and it is possible to work with either microcanonical, canonical or grand-canonical ensembles. In this respect, a thermodynamic analysis is better suited for such systems than for standard 3D gravitational systems, where the potential energy is unbounded from below and stable equilibria do not always exist, and different statistical ensembles are not equivalent [33].

We work in the grand-canonical ensemble, where the dark matter particles are confined in a box of size x (the scale $x_{\rm coll}(z)$ that is turning non-linear at redshift z), with a mean temperature $T = 1/\beta$ and chemical potential μ that are set by the initial velocity scale $c_{\rm coll}(z)$ and mean density $\bar\rho(z)$. The analysis of the thermodynamic equilibria and phase transitions is described in details in the companion paper [14]. The main result is that at high temperature, $T > T_c$ and $\beta < \beta_c$, the thermodynamic equilibrium is homogeneous, whereas at low temperature, $T < T_c$ and $\beta > \beta_c$, the equilibrium is inhomogeneous. Indeed, at high temperature the system is dominated by its kinetic energy and the potential energy associated with the fifth force (which is bounded) is negligible, so that we recover a perfect gas without interactions, whereas at low temperature the fifth-force potential becomes important and leads to strong inhomogeneities as it corresponds to an attractive force. In terms of the rescaled dimensionless variables θ and $\hat\beta$,

$$\theta = \ln\left(\frac{\rho}{\rho_\alpha}\right), \quad \hat\beta = \alpha c^2 \beta, \tag{144}$$

this leads to the phase diagram shown in Fig. 12. The equilibrium is inhomogeneous inside the shaded region, which is limited at low $\hat\beta$ by the inverse critical temperature $\hat\beta_c$, with $\hat\beta_c \simeq \{6.85, 5.58, 5.14\}$ for $\zeta = \{1/2, 1, 3/2\}$. The upper and lower limits of the domain are the curves $\theta_+(\hat\beta)$ and $\theta_-(\hat\beta)$, which obey the low-temperature asymptotes

$$\hat\beta \to \infty: \quad \theta_+ \sim \frac{1+\zeta}{\zeta}\ln\hat\beta, \quad \theta_- \sim -\hat\beta. \tag{145}$$

Then, if the average initial temperature and density $(1/\hat\beta, \theta)$ fall outside the shaded domain the system remains homogeneous. If they fall inside the shaded domain the system becomes inhomogeneous and splits over two domains with density θ_- and θ_+, with a proportion such that the total mass is conserved. Because of the ultra-local property [i.e. $\ln A$ is a local function through $\rho(\mathbf{x})$], the equilibrium factorizes over space $\mathbf{x}$ so that the two domains at density $\theta_\pm$ are not necessarily connected and can take any shape.

The solid curves in Fig. 12 are the cosmological trajectories associated with the scale and velocity $\{x_{\rm coll}(z), c_{\rm coll}(z)\}$ displayed in Fig. 11, which correspond to

$$\theta_{\rm coll}(z) = \ln\left(\frac{\bar\rho(z)}{\rho_\alpha}\right), \quad \hat\beta_{\rm coll}(z) = \frac{\alpha c^2}{c_{\rm coll}^2(z)}. \tag{146}$$

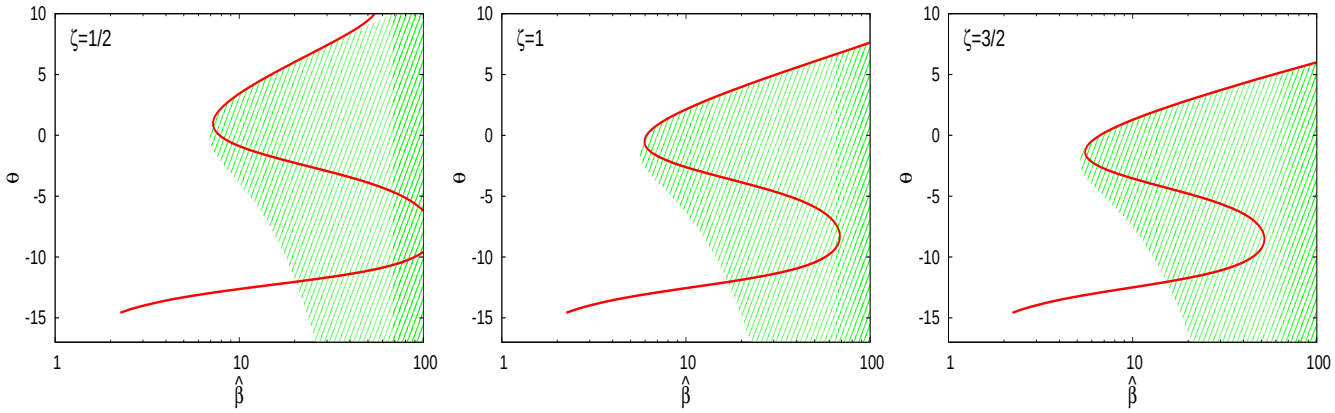

FIG. 12: Thermodynamic phase diagram for the ultra-local models with $\zeta = 1/2, 1$ and $3/2$. The shaded area is the region of initial inverse temperature $\hat{\beta}$ and density θ where the thermodynamic equilibrium is inhomogeneous. The solid line is the cosmological trajectory $(\hat{\beta}_{\rm coll}(z), \theta_{\rm coll}(z))$.

This trajectory moves downward to lower densities with cosmic time, following $\bar{\rho}(z)$. In agreement with the lower panel of Fig. 11, the inverse temperature $\hat{\beta}_{\rm coll}$ first decreases until a_α, as the velocity $c_{\rm coll}(z)$ grows. Next, $\hat{\beta}_{\rm coll}$ increases while $c_{\rm coll}(z)$ decreases along with the fifth force, until we recover the $\Lambda-$CDM behavior at late times and $\hat{\beta}_{\rm coll}$ decreases again thereafter. We are interested in the first era, $a < a_\alpha$, and we find that the cosmological trajectory is almost indistinguishable from the upper boundary $\theta_+(\hat{\beta})$ of the inhomogeneous thermodynamic phase. Indeed, at early times we have $c_{\rm coll} \simeq c_s$, hence $\hat{\beta}_{\rm coll} \simeq \alpha/\epsilon_1$ from Eq.(140). Using Eq.(104) we have at high densities, which also correspond to $a < a_\alpha$, $\epsilon_1 \sim \alpha(\rho/\rho_\alpha)^{-\zeta/(1+\zeta)} = \alpha e^{-\zeta\theta/(1+\zeta)}$, hence

$$a \ll a_\alpha : \quad \theta_{\rm coll} \sim \frac{1+\zeta}{\zeta} \ln \hat{\beta}_{\rm coll}, \tag{147}$$

and we recover the asymptote (145) of $\theta_+(\hat{\beta})$.

If $\theta_{\rm coll} > \theta_+$ we are in the homogeneous phase and the system remains at the initial density $\bar{\rho}$. If $\theta_{\rm coll} \lesssim \theta_+$ we are in the inhomogeneous phase and the system splits over regions of densities θ_+ and θ_-. However, as we remain close to θ_+ most of the volume is at the density $\theta_+ \simeq \theta_{\rm coll}$ and only a small fraction of the volume is at the low density θ_-. Neglecting these small regions, we can consider that in both cases the system remains approximately homogeneous. This means that, according to this thermodynamic analysis, the cosmological density field does not develop strong inhomogeneities that are set by the cutoff scale of the theory when it enters the fifth-force non-linear regime. Therefore, density gradients remain set by the large-scale cosmological density gradients and the analysis of the linear growing modes and of the spherical collapse presented in previous sections are valid. On small non-linear scales and at late times, where Newtonian gravity becomes dominant, we recover the usual gravitational instability that we neglected in this analysis and structure formation proceeds as in the standard Λ-CDM case.

C. Halo centers

It is interesting to apply the thermodynamic analysis presented above to the inner radii of clusters and galaxies. Indeed, we have seen in section V A 1 that the fifth force becomes large inside spherical halos and the ratio $F_A/F_{\rm N}$ actually diverges at the center for shallow density profiles, see Fig. 8 and Eq.(127). However, this analysis was based on dimensional and scaling arguments and it fails if the density field becomes strongly inhomogeneous so that the typical density inside the halo is very different from the global averaged density. The thermodynamic analysis used to derive the phase space diagram shown in Fig. 12 neglected Newtonian gravity. However, we can also apply its conclusions to a regime dominated by Newtonian gravity where at radius r inside the halo the structures built by gravity and the density gradients are on scale r. Then, we can ask whether at this radius r fifth-force effects may lead to a fragmentation of the system on much smaller scales $\ell \ll r$. To study this small-scale behavior we can neglect the larger-scale gravitational gradients r and discard gravitational forces.

Within a radius r inside the halo the averaged reduced density and inverse temperature are

$$\theta_r = \ln\left(\frac{\rho_<(r)}{\rho_\alpha}\right), \quad \hat{\beta}_r = \frac{\alpha c^2}{{\rm Max}(c_s^2, v_{\rm N}^2)}, \tag{148}$$

where $v_{\rm N}$ is the Newtonian circular velocity and c_s is the fifth-force velocity scale defined in Eq.(122). As seen in Eq.(123), the maximum ${\rm Max}(c_s^2, v_{\rm N}^2)$ shifts from one velocity scale to the other when the associated force becomes dominant. Here we choose the non-analytic interpolation ${\rm Max}(c_s^2, v_{\rm N}^2)$ instead of the smooth interpolation

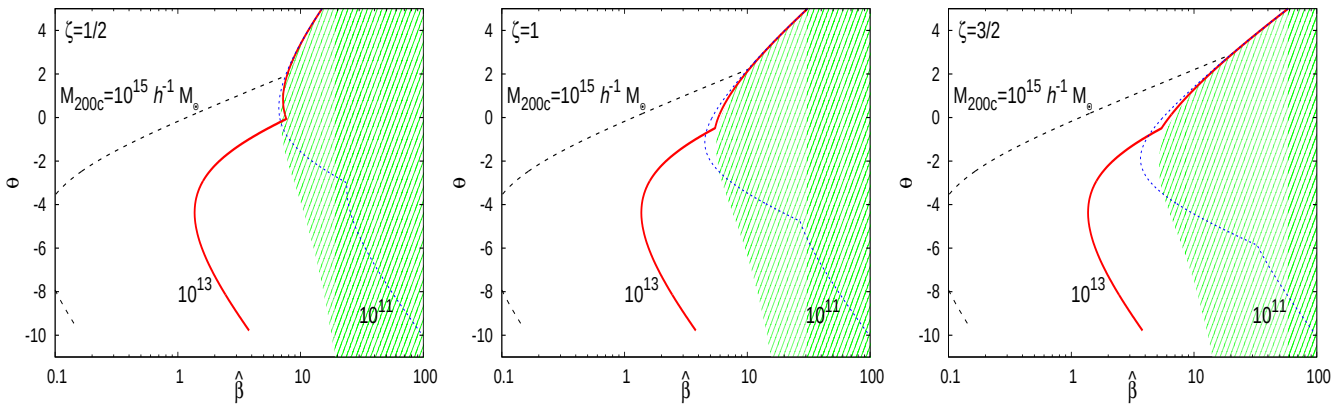

FIG. 13: Radial trajectory $(\hat{\beta}_r, \theta_r)$ over the thermodynamic phase diagram inside NFW halos of mass $M = 10^{15}, 10^{13}$ and $10^{11} h^{-1} M_\odot$. at $z = 0$.

$c_s^2 + v_{\rm N}^2$ that we used in Eq.(139) for the cosmological analysis for illustrative convenience. Indeed, the discontinuous changes of slope in Fig. 13 show at once the location of the transitions $|\eta| = 1$ between the fifth-force and Newtonian gravity regimes.

When the density grows at small radii as a power law, $\rho \propto r^{-\gamma_p}$, we have seen in Eq.(127) that the fifth-force to gravity ratio η behaves as $\eta \sim r^{\gamma_p(1+2\zeta)/(1+\zeta)-2}$ with

$$v_{\rm N}^2 \sim r^{2-\gamma_p}, \quad c_s^2 \sim r^{\gamma_p \zeta/(1+\zeta)}, \tag{149}$$

at high density $\rho \gg \rho_\alpha$, where we used Eq.(101). This gives in the Newtonian gravity and fifth-force regimes

$$|\eta| < 1 : \quad \theta_r \sim \frac{\gamma_p}{2-\gamma_p} \ln \hat{\beta}_r, \tag{150}$$

$$|\eta| > 1 : \quad \theta_r \sim \frac{1+\zeta}{\zeta} \ln \hat{\beta}_r. \tag{151}$$

For $\gamma_p > 2$ we are in the Newtonian regime $v_{\rm N}^2 \to \infty$, $\hat{\beta}_r \to 0$, so that we are in the homogeneous phase of the thermodynamic phase diagram as $\hat{\beta}_r < \hat{\beta}_c$. For $(2+2\zeta)/(1+2\zeta) < \gamma_p < 2$ Newtonian gravity still dominates at small radii and we have the asymptote (150) with $\gamma_p/(2-\gamma_p) > (1+\zeta)/\zeta$, so that the radial trajectory $(\hat{\beta}_r, \theta_r)$ moves farther above from the upper bound θ_+ of Eq.(145) of the inhomogeneous phase and small radii are within the homogeneous phase. For $\gamma_p < (2+2\zeta)/(1+2\zeta)$ we are in the fifth-force regime and we obtain $\theta_r \sim \theta_+$, so that the radial trajectory $(\hat{\beta}_r, \theta_r)$ follows the upper boundary of the inhomogeneous phase domain. This means that the dimensional analysis of section V A 1 is valid as the fifth force does not push towards a fragmentation of the system down to very small scales.

These asymptotic results apply to the small-radius limit $r \to 0$. In Fig. 13 we show the full radial trajectories $(\hat{\beta}_r, \theta_r)$ over the thermodynamic phase diagram, from R_{200c} inward, for the NFW halos that were displayed in Fig. 8 at $z = 0$. As we move inside the halo, towards smaller radii r, the density θ_r grows and the trajectory moves upward in the figure. The turn-around of $\hat{\beta}_r$ at $\theta_r \simeq -4$ corresponds to the NFW radius r_s where the local slope of the density goes through $\gamma = 2$ and the circular velocity is maximum. At smaller radii, $r \ll r_s$, the NFW profile goes to $\rho \propto r^{-1}$, hence $\gamma_p = 1$. In agreement with the asymptotic analysis above, this implies that we move farther into the fifth-force regime and we follow the upper boundary θ_+ of the inhomogeneous phase domain, so that the dimensional analysis of section V A 1 is valid. This also leads to an increasingly dominant fifth force at small radii and characteristic velocities that are higher than the Newtonian circular velocity. This may rule out these ultra-local scenarios. However, on small scales the baryonic component is non-negligible and it actually dominates on kpc scales inside galaxies. Since the baryons do not feel the fifth force this could keep these models consistent with observations. On the other hand, for low-mass halos, $M \lesssim 10^{11} h^{-1} M_\odot$ at $z = 0$, we find that a significant part of the halo is within the inhomogeneous thermodynamic phase. This may leave some signature as a possible fragmentation of the system on these intermediate scales into higher-density structures. This process would next lead to a screening of the fifth force, because of the ultra-local character of the fifth force. Indeed, because it is set by the local density gradients, the fragmentation of the system leads to a disappearance of large-scale collective effects and the fifth force behaves like a surface tension at the boundaries of different domains. Such a process may also happen in the case of massive halos at earlier stages of their formation, which could effectively screen the fifth force whereas the simple static analysis leads to a dominant fifth force at small radii. However, a more precise analysis to follow such evolutionary tracks and check the final outcomes of the systems requires numerical studies that are beyond the scope of this paper.

VII. DEPENDENCE ON THE α PARAMETER

In this section we investigate how the results obtained in the previous sections change when we vary the parameter α. As a matter of example, we consider the model with $\zeta = 1$ and we show our results in Fig. 14, where we compare the case $\alpha = 10^{-6}$ considered in the previous sections with the two cases $\alpha = 10^{-7}$ and $\alpha = 10^{-8}$.

In agreement with the discussion in section IV B, as α decreases the maximum amplitude of ϵ_1 decreases as $\epsilon_1(a_\alpha) \sim \alpha$ while the associated scale factor decreases as $a_\alpha \sim \alpha^{1/3}$. This implies that the effect of the fifth force is shifted to higher redshift with a lower amplitude, whence a smaller impact of the scalar field on the matter power spectrum, $P(k, z)$, and on the halo mass function, as we can check in the upper right and lower left panels in Fig. 14. The area in the (M, R) plane where the fifth force is greater than Newtonian gravity also shrinks as α decreases, as we can see in the lower right panel. This is because $R_\alpha \propto \alpha$, which moves the upper branch down towards small radii, whereas the lower branch slowly moves upward because at fixed mass we have $R(M) \sim \alpha^{-1/(4\zeta+1)}$. Therefore, galaxies are no longer sensitive to the modification of gravity if $\alpha \lesssim 5 \times 10^{-7}$.

VIII. CONCLUSION

We have considered in this paper supersymmetric chameleon models with a very large mass, $1/m_{\rm eff} \ll 10^{-4}$mm, and coupling $\beta \gg 1$. This makes the range of the fifth force very small and leads to an equivalence between these supersymmetric chameleon models and the ultra-local models studied in a companion paper, for cosmological scales with $H \ll k/a \ll m_{\rm eff}$. The background remains very close to the Λ-CDM cosmology in both sets of models. However, in contrast with the more general ultra-local models, in this supersymmetric context only the dark matter is sensitive to the fifth force. Therefore, although the ultra-local character of the models gives rise to an automatic screening mechanism that ensures that we satisfy Solar System tests of gravity in that more general framework, in the context studied in this paper this mechanism is not so critical as baryons, which dominate on small scales and in the Solar System, never feel the fifth force (except through its effects on the dark matter Newtonian potential) and follow General Relativity.

We have first described how to build such chameleon models in this supersymmetric context. This involves several characteristic functions that enter the Kähler potential K, which governs the kinetic terms of the model, the superpotential W responsible for the interactions between the fields, and the coupling between the dark matter and the dark energy. This also introduces several energy scales that may be different. We have shown in details how these models are equivalent to ultra-local models for cosmological purposes. This leads to a great simplification as the latter involve a single free function, $\ln A(\tilde{\chi})$. As in most dark energy and modified gravity models, we also need to introduce a cosmological constant and the associated energy scale. In addition, we need a small parameter $\alpha \lesssim 10^{-6}$, which however appears as a ratio of several energy scales. This provides a natural setting to explain why this quantity can be significantly different from unity.

Next, we have used the ultra-local models identification to study the cosmological properties of these scenarios. We have considered both the background dynamics and the evolution of linear perturbations. Whereas the background remains very close to the Λ-CDM evolution, within an accuracy of 10^{-6}, the growth of cosmological structures is significantly amplified on scales below $1h^{-1}$Mpc. This fifth-force effect shows a fast increase at high k as it corresponds to a pressure-like term in the linearized equations of motion. Another property that is peculiar to these models, as opposed to most dark energy or modified gravity models, is that the fifth force is the greatest at a high redshift $z_\alpha \sim \alpha^{-1/3} \sim 100$ and for galaxies (among cosmological structures).

We have also considered the modifications to the spherical collapse of cosmological structures. The faster growth of structures at $z \sim z_\alpha$ leads to an acceleration of the collapse at these early times and to a lower linear density threshold $\delta_L^{\Lambda-\rm CDM}$ required to reach a non-linear density contrast of 200 today, especially on smaller scales where the fifth force is greater. This leads to a higher halo mass function at intermediate masses, $10^8 \lesssim M < 10^{14}h^{-1}M_\odot$, as compared with the Λ-CDM cosmology. Next, we have considered the behavior of the fifth force inside spherical halos. We find that the fifth force increasingly dominates at smaller radii in halos with a shallow density profile, $\gamma_p \lesssim 1$, as for NFW profiles. On the other hand, the fifth force is negligible on cluster scales and of the same order as Newtonian gravity on galaxy scales. This suggests that galaxies could be the best probes of such models.

To investigate the non-linear fifth force regime, and to check that the previous cosmological analysis is not violated by small-scale non-linear effects, we have used the thermodynamic analysis developed in the companion paper. Again, we find that for these supersymmetric chameleon models the cosmological scales that turn non-linear at high redshift because of the fifth force are at the boundary of the inhomogeneous domain in the thermodynamic phase diagram. This suggests that they do not develop strong small-scale inhomogeneities and that the standard mean field cosmological analysis is valid. The same behavior is found at small radii in spherical halos, which again suggests that the spherically averaged analysis applies. However, for low-mass halos, $M \lesssim 10^{11}h^{-1}M_\odot$ at $z = 0$, intermediate radii fall within the inhomogeneous phase. This could lead to some fragmentation of the system with the formation of intermediate mass clumps. On the other hand, this same process leads to a self-screening of the fifth force as isolated

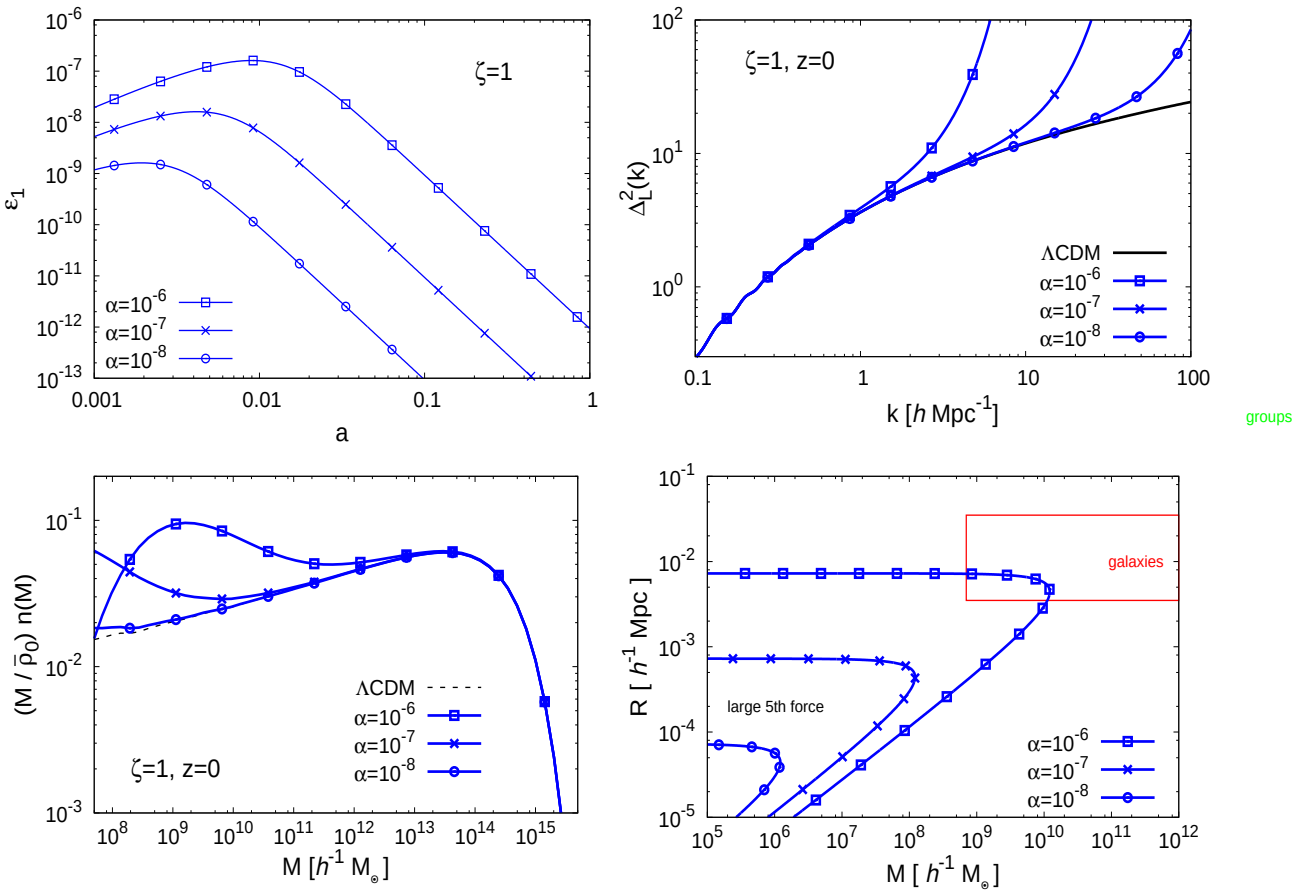

FIG. 14: Dependence on the parameter α of the deviations from the Λ-CDM predictions. We plot models with $\zeta = 1$ and $\alpha = 10^{-6}$, 10^{-7} and 10^{-8}. *Upper left panel:* $\epsilon_1(a)$ as a function of the scale factor, as in Fig. 2. *Upper right panel:* logarithmic linear power spectrum $\Delta^2_L(k, z)$ at redshift $z = 0$, as in Fig. 4. *Lower left panel:* halo mass function as in the lower panel of Fig. 7. *Lower right panel:* domain in the mass-radius plane where the fifth force is greater than Newtonian gravity, as in Fig. 10.

clumps no longer interact through the fifth force because of its ultra-local character. Finally, we have considered the dependence of our results on the value of the parameter α. We find that for $\alpha \ll 10^{-7}$ the deviations from the Λ-CDM cosmology are likely to be negligible (contrary to the models studied in the companion paper) because they have a lower amplitude and are pushed to lower scales where baryons are dominant.

Thus, we find that although such models follow the Λ-CDM behavior at the background level they display a non-standard behavior for the dark matter perturbations on small scales, below $1h^{-1}$Mpc. At the level of the preliminary analysis presented in this paper they appear to remain globally consistent with observational constraints. However, the effects of the fifth force deep inside halos, on kpc scales, may provide strong constraints and rule out this models. In particular, the thermodynamic analysis presented in this paper may not be sufficient as the systems may not reach this equilibrium because of incomplete relaxation. To go beyond the analytic approaches used in this paper and to make an accurate comparison with data on galaxy scales requires numerical simulations, which we leave to future work.

Acknowledgments

This work is supported in part by the French Agence Nationale de la Recherche under Grant ANR-12-BS05-0002. This project has received funding from the European Unions Horizon 2020 research and innovation programme under the Marie Skodowska-Curie grant agreement No 690575.

[1] A. G. Riess et al. (Supernova Search Team), Astron.J. **116**, 1009 (1998), astro-ph/9805201.

[2] S. Perlmutter et al. (Supernova Cosmology Project), Bull.Am.Astron.Soc. **29**, 1351 (1997), astro-ph/9812473.

[3] E. J. Copeland, M. Sami, and S. Tsujikawa, Int.J.Mod.Phys. **D15**, 1753 (2006), hep-th/0603057.

[4] A. Joyce, B. Jain, J. Khoury, and M. Trodden, Phys. Rept. **568**, 1 (2015), 1407.0059.

[5] W. Hu and I. Sawicki, Phys. Rev. **D76**, 064004 (2007), 0705.1158.

[6] A. Nicolis, R. Rattazzi, and E. Trincherini, Phys.Rev. **D79**, 064036 (2009), 0811.2197.

[7] G. W. Horndeski, Int.J.Theor.Phys. **10**, 363 (1974).

[8] J. D. Bekenstein, Phys. Rev. **D48**, 3641 (1993), gr-qc/9211017.

[9] J. Khoury and A. Weltman, Phys. Rev. **D69**, 044026 (2004), astro-ph/0309411.

[10] T. Damour and A. M. Polyakov, Nucl. Phys. **B423**, 532 (1994), hep-th/9401069.

[11] E. Babichev, C. Deffayet, and R. Ziour, Int.J.Mod.Phys. **D18**, 2147 (2009), 0905.2943.

[12] P. Brax and P. Valageas, Phys. Rev. D **90**, 023507 (2014), 1403.5420.

[13] A. Vainshtein, Phys.Lett. **B39**, 393 (1972).

[14] P. Brax, L. A. Rizzo, and P. Valageas (2016), 1605.02938.

[15] P. Brax, Phys.Lett. **B712**, 155 (2012), 1202.0740.

[16] C. de Rham and R. H. Ribeiro, JCAP **1411**, 016 (2014), 1405.5213.

[17] P. Brax and J. Martin, Phys. Lett. **B468**, 40 (1999), astro-ph/9905040.

[18] P. Brax, C. van de Bruck, J. Martin, and A.-C. Davis, JCAP **0909**, 032 (2009), 0904.3471.

[19] P. Brax, A.-C. Davis, and J. Sakstein, JCAP **1310**, 007 (2013), 1302.3080.

[20] P. Brax, A.-C. Davis, and J. Sakstein, Phys. Lett. **B719**, 210 (2013), 1212.4392.

[21] S. M. Carroll, I. Sawicki, A. Silvestri, and M. Trodden, New J. Phys. **8**, 323 (2006), astro-ph/0607458.

[22] P. Binetruy, *Supersymmetry: Theory, experiment and cosmology* (2006).

[23] B. Ratra and P. J. E. Peebles, Phys. Rev. **D37**, 3406 (1988).

[24] P. Fayet, Phys. Lett. **B175**, 471 (1986).

[25] P. Brax, C. van de Bruck, A.-C. Davis, J. Khoury, and A. Weltman, Phys. Rev. **D70**, 123518 (2004), astro-ph/0408415.

[26] P. Brax, C. van de Bruck, A.-C. Davis, and A. M. Green, Phys.Lett. **B633**, 441 (2006), astro-ph/0509878.

[27] P. Brax, A.-C. Davis, B. Li, and H. A. Winther (2012), 1203.4812.

[28] W. H. Press and P. Schechter, Astrophys. J. **187**, 425 (1974).

[29] J. F. Navarro, C. S. Frenk, and S. D. M. White, Astrophys. J. **462**, 563 (1996), astro-ph/9508025.

[30] P. H. Chavanis, J. Vatteville, and F. Bouchet, European Physical Journal B **46**, 61 (2005), arXiv:cond-mat/0408117.

[31] R. Balian, *From Microphysics to Macrophysics*, Theoretical and Mathematical Physics (Springer-Verlag, Berlin, Germany, 2007), ISBN 978-3-540-45469-4, URL `http://www.springer.com/fr/book/9783540454694`.

[32] D. Lynden-Bell, *Mon. Not. R. Astr. Soc.* **136**, 101 (1967).

[33] T. Padmanabhan, *Phys. Rep.* **188**, 285 (1990).

[34] Although the vacuum energy due to V_D lifts the vanishing energy density of a true supersymmetric minimum and therefore supersymmetry is broken by ξ, we will still refer to $\varphi_{\rm min}$ as the supersymmetric minimum as it minimises V_F.